1-1-2009

Flat-cladding fibre bragg grating sensors for large strain fatigue tests

Cheng Li
Ryerson University

FLAT-CLADDING FIBER BRAGG GRATING SENSORS FOR LARGE STRAIN FATIGUE TESTS

by

Cheng Li

B. Eng., Southwest Jiaotong University, P.R.China, 1998

A thesis

presented to Ryerson University

in partial fulfillment of the

requirement for the degree of

Master of Applied Science

in the Program of

Electrical and Computer Engineering

Toronto, Ontario, Canada, 2009

Author's Declaration

I hereby declare that I am the sole author of this thesis.

I authorize Ryerson University to lend this thesis to other institutions or individuals for the purpose of scholarly research.

I further authorize Ryerson University to reproduce this thesis by photocopying or by other means, in total or in part, at the request of other institutions or individuals for the purpose of scholarly research.

Abstract

Flat-cladding fiber Bragg grating sensors for large strain fatigue tests

© Cheng Li, 2009

Master of Applied Science

Electrical and Computer Engineering

Ryerson University

In the design of mechanical components, the fatigue properties of material are of particular importance as ~80 % of metal failures in practice arise from fatigue. The fatigue life is generally determined from low cyclic fatigue tests at large strain. This thesis developed a novel flat-cladding Fiber Bragg Grating sensor array applied in the characterization of LCF properties of three different specimens. With a new bonding process, large strain amplitude measurement of up to ±8000 με was achieved in the Aluminum base metal and asymmetric hysteresis loops at high strain amplitudes due to twinning in compression and subsequent detwinning in tension was observed in Magnesium alloy. Moreover, an abnormal softening and hardening variation in different zone of friction stir welded Aluminum alloy was discovered through the FBG sensor distribution. The validity shows that the FBG sensor a vital tool in the LCF tests at large strain amplitudes. Furthermore, due to its small size, the multiplexed FBG sensor array could also be applied to the measurements of strain distribution.

Keywords: Flat-cladding optical fiber sensor; Fiber Bragg Grating (FBG); Low cycle fatigue (LCF); Friction stir welding (FSW); Plastic deformation; Twinning and

Detwinning.

Acknowledgements

I would like to take this opportunity to express my gratitude to my supervisor, Prof. Xijia Gu, who offered me a great opportunity and guidance to research in the field of optical fiber technology. His enthusiasm for science and tireless attention to the research work has set me an icon and motivated me throughout my years at Ryerson University. I would like to thank him also for the financial support to complete my graduate studies.

I would like to thank Prof. Daolun Chen for not just dedicated in sharing his knowledge in the field of mechanical engineering, but also offered me countless help in designing and preparing experiments.

I would like to thank Mrs Jiang Li, who gave me the guidance on fiber Bragg grating fabrication and great help in preparing experiments. I also would like to thank Dr. Aihan Feng, who collaborated with me in my research. Through discussions with her, I gained better understandings in fatigue properties of metals.

Finally, I would like to express my deepest gratitude to my family, specially my parents who are living in the countryside of China. I also would like to thank my wife Peilin Yu. Without her patient understandings and support, I could not finish my studies smoothly and effectively.

Table of Contents

List of Figures

1 Introduction

1.1 Perspective

For reducing the fuel consumption and greenhouse gas emission, the low density metals, such as aluminum and magnesium (2.7 gm/cc and 1.7 gm/cc vs 7.8 gm/cc for steel) alloys, have gained more attractive than the conventional structural materials due to their high strength-to-weight ratios and specific strength [1-6].

The fatigue life of mechanical components is generally determined from low cyclic fatigue tests at large strain amplitudes and high cyclic fatigue tests at low strain amplitudes [7]. To accurately predict the fatigue life, it is critical to measure the strain in push-pull fatigue tests, especially under the large strain amplitude that induces significant plastic deformation. However, the conventional thin-film strain gauge can not take large cyclic strain amplitude [8]; and the extensometer, though capable of taking large strain amplitude, is relatively large in size, unsuitable for the strain measurements at boundary of dissimilar materials or for localized strain measurements [9].

Fiber optic sensor, particularly Fiber Bragg Grating (FBG) has gained popularity in the last decade due to its wide dynamic range, immune to electromagnetic interference and its multiplexing capability [10]. FBG sensor of 125 μm in diameter could be made as short as 2 to 5 mm in length and was used recently in localized strain measurements [11]. Despite the success of FBG in strain sensing and structure health monitoring, there are few reports of its application in metal fatigue tests, especially in large cyclic strain amplitude tests. When a FBG fiber is bonded to a substrate with epoxy, the substrate strain is transferred to fiber sensor by shear stress of epoxy. Due to the limited contact area between a circular fiber and a flat substrate and shear modulus of the epoxy, large substrate strain would cause the fiber to slip, rendering the FBG strain reading to be less than the true substrate strain [12]. Typically the FBG sensor is used when the strain variation is less than 3000 με [13]. In order to overcome this limitation, a new type of FBG sensor and bonding process are developed for the measurements of large strain amplitudes in fatigue tests and other material tests such as crack-initiation detection and crack closure evaluation.

In this thesis, we report the development of a flat-cladding FBG sensor and a bonding process that significantly extended the measurement range of strain amplitudes. We demonstrate that the sensor can measure reliably the large strain amplitudes of up to ± 8000 με in the base metal. Further applications of this FBG sensor in the fatigue tests of aluminum and magnesium alloy samples are also presented. An asymmetric hysteresis loops at high strain amplitudes due to twinning in compression and subsequent detwinning in tension was observed in Magnesium alloy. Moreover, nonuniform softening and hardening variation in the different zones of a friction stir welded Aluminum alloy was discovered through the distributed FBG sensors. The validity of the new method shows that the FBG sensor could be a vital tool in the low cyclic fatigue tests at large strain amplitude. Furthermore, due to its small size, the FBG sensors could be used to measure the localized strain variations, for example, the welding joints, detect fatigue crack initiation, and determine crack closure effect during fatigue crack propagation. Last but not the least, the multiplexed FBG sensors array could also be applied to the measurements of strain distribution in composite materials and mechanical components, as well as for structure health monitoring.

1.2 Thesis Overview

Chapter 2: This chapter reviews the characteristics of photosensitivity; describes the properties of fiber Bragg gratings by solving coupled-mode equation; introduces the techniques for fabricating Bragg gratings in optical fiber, especially the phase mask method; illustrates some applications fiber Bragg grating sensor and demonstrates the principle of fiber Bragg gratings sensor, such as strain and temperature.

Chapter 3: This chapter explains cyclic softening and hardening by introducing cyclic stress-strain curve; emphasizes the importance of the low-cycle fatigue (LCF) to fatigue failure and fatigue life.

Chapter 4: This chapter describes experimental preparation and configuration, which include FBG and specimen fabrication, the process of bonding FBG to the specimen and strain-controlled fatigue testing system.

Chapter 5: This chapter presents and analysis the data gathered from the experiments conducted on three different type of specimens-base metal of aluminum alloy, FSWed aluminum alloy and magnesium alloy; discusses the possible reasons and the consequent applications

Chapter 6: Conclusion and Future Work. The closure discusses the final remarks in regards to the experimental works as well as the improvement for the future studies.

Reference

1. J.E. Hatch: *Aluminum: Properties and Physical Metallurgy*, ASM, 1984.

2. A. Kelkar, R. Roth, J. Clark, "Automobile bodies: Can aluminum be an economical alternative to steel?", *JOM*, vol.53(8), pp.28-32, 2001

3. K.U. Kainer: *Magnesium Alloys and Technology*, Wiley-VCH, Cambridge, United Kingdom, 2003.

4. A.A. Luo, "Magnesium: Current and potential automotive applications", *JOM,* vol.54(2), pp.42-48, 2002.

5. A.A. Luo: *SAE 2005 Transactions-Journal of Materials and Manufacturing*, SAE, Warrendale, PA, pp.411-421, 2005.

6. H.E. Fredrich and B.L. Mordiker: *Magnesium Technology-Metallurgy, Design Data, Applications*, Springer-Verlag, Berlin, Germany, 2006

7. G.E. Dieter, *Mechanical Metallurgy*, McGraw-Hill, 1986.

8. B.G. Lipiák, *Instrument Engineers' Handbook: Process Measurement and Analysis*, CRC Press, pp.1122, 2009.

9. G.F. Lucas, P.C. McKeighan and J.S. Ransom: *Nontraditional Methods of Sensing Stress, Strain and Damage in Materials and Structures,* ASTM International, pp.29-39, 2001.

10. M. Bass and E.W.V. stryland: *Fiber Optic Handbook: Fiber, Devices, and Systems for Optical Communications*, OSA, McGraw-Hill, 2002.

11. H. Lu, R. Hussain, M. Zhou and X. Gu, "Fiber Bragg Grating Sensors for Failure Detection of Flip Chip Ball Grid Array in Four-Point Bend Tests", IEE Sensors Journal, vol.9(4), pp.457-463, 2009.

12. W.Y. Li, C.C. Cheng and Y.L. Lo, "Investigation of strain transmission of surface-bonded FBGs used as strain sensors", Sensors and Actuators A, vol.149, pp.201-207, 2009.

13. D.C. Betz, G. Thursby, B.C. Culshaw and W.J. Staszewski, "Advanced layout of a fiber Bragg grating strain gauge rosette", J. Lightwave Technology, vol.24(2), pp.1019-1026, 2006.

2 Fiber Bragg Grating

2.1 Introduction

Optical fiber sensors have now been with us for at least 40 years, and much has happened since the Fotonic Probe made its tentative appearance in the mid 1960s [1]. Due to its attractive advantages of high dynamic range, immune to electromagnetic interference and multiplexing capability, the optical fiber sensors have been widely extolled in both research literature and real commercial successes. There are several implementations of fiber-optic sensors - FBG sensors, FP (Fabry–Pérot) interferometric sensors, TM (two-mode) fiber-optic sensors and PM (polarimetric) fiber-optic sensors [2]. Compared with other fiber-optic sensors, advantages of FBG sensors over competing technologies include all-fiber geometry, low insertion loss and low cost, making FBG an ideal device for optical fiber sensors.

In 1978, at the Communications Research Council of Canada, (CRC) Ottawa, Ontario, Canada, K.O. Hill et al. [3,4] first demonstrated periodic refractive index changes in a germanosilica optical fiber by launching a laser beam into a fiber. However, it did not receive great attention as the grating was formed by the standing-wave interference pattern, set up by counter-propagating beams of light at 488 nm or 514.5 nm, from an Argon-ion laser. The grating resonance is at the wavelength of the writing laser, which greatly limited its application. Subsequent investigations revealed that the photoinduced index depended on the square of the writing power, which suggested a two-photon process at the blue/green writing wavelength [5]. The grating became a popular device starting from the work of Meltz et al. [6] in 1989, dramatically improving the writing efficiency by demonstrating the possibility for fabricating gratings at a selected Bragg wavelength, simply by adjusting the angle between the intercepting ultraviolet (UV) laser beams. Since then, interest and activity in the field have increased rapidly to the point where fabrication methods have been significantly refined; many different fiber types have been used for grating fabrication, including several non-germanosilicate compositions. FBG is one of the key components in modern optical fiber communications and sensor systems. The commercial products of FBG have been available since early 1995. Many applications have been identified and demonstrated, and the gratings are now available commercially from several suppliers.

This chapter reviews the characteristics of photosensitivity, the properties of Bragg gratings, the techniques for fabricating Bragg gratings in optical fiber, fiber Bragg gratings sensor and some FBG sensor applications.

2.2 Photosensitivity

Fiber photosensitivity was first observed in the experiment that continuous wave blue (488 nm) light from an Argon-ion laser is launched into a short piece of nominally single mode optical fiber [3]. The intensity of the light reflected back from the fiber grew in strength until it saturated (with >90% reflectivity). It was explained in terms of "photosensitivity" which was known as the capability of light to induce permanent refractive index changes in the core of an optical fiber, normally by the exposure of fiber core to an intense optical interference pattern of ultraviolet light.

When ultraviolet light irradiates onto an optical fiber, the refractive index of the fiber is changed permanently in the sense that it will last for several years (lifetimes of 25 years are predicted) if the optical fiber after exposure is annealed appropriately; for example, by heating for a few hours at a temperature of 150 $^{\text{o}}$ [7]. Initially, photosensitivity was not only associated with germanium-doped optical fibers, but also has been observed in a wide variety of different fibers, many of which do not contain germanium as dopant. Nevertheless, optical fiber with a germanium-doped core remains the most important material for the fabrication of FBG.

The magnitude of the photoinduced refractive index change (Δn) obtained depends on several different factors: the irradiation conditions (wavelength, intensity, and total dosage of irradiating light), the composition of glassy material forming the fiber core, and any processing of the fiber prior and subsequent to irradiation. A wide variety of different continuous wave and pulsed-laser light sources, with wavelengths ranging from the visible to the vacuum ultraviolet, have been used to photoinduce refractive index changes in optical fibers. In practice, the most commonly used light sources are KrF and ArF excimer lasers that generate, respectively, 248 nm and 193 nm light pulses (pulse width ~10 ns) at pulse repetition rates of 20 to 50 pps. Typically, the fiber core is exposed to laser light for a few minutes at pulse energy levels ranging from 100 to 1000 mJ cm^{-2} $pulse^{-1}$. Under these conditions, Δn is positive in germanium doped single mode fiber with a magnitude ranging between 10^{-5} and 10^{-3}. Techniques such as hydrogen loading [8] or flame brushing [9] are available which can be used to process the fiber prior to irradiation in order to enhance the refractive index change obtained on irradiation. For example, a Δn as high as 10^{-2} has been obtained by the use of hydrogen loading.

Irradiation at intensity levels higher than 1000 mJ cm^{-2} marks the onset of a different nonlinear photosensitive process that enables a single irradiating excimer light pulse to photoinduce a large index change in a small localized region near the core/cladding boundary of the fiber. In this case, the refractive index changes are sufficiently large to be observable with a phase contrast microscope and have the appearance of physically damaging the fiber. This phenomenon has been used for the writing of gratings using a single excimer light pulse.

Another property of the photoinduced refractive index change is anisotropy. This characteristic is most easily observed by irradiating the fiber from the side with ultraviolet light that is polarized perpendicular to the fiber axis. The anisotropy in the photoinduced refractive index change results in the fiber becoming birefringent for light propagating through the fiber. The effect is useful for fabricating polarization mode-converting devices or rocking filters [10].

Although the mechanism of photosensitivity still remains unclear and the details of the processes are not yet fully resolved, the origin of the photosensitivity of Ge-doped silica fiber is understood to be linked with the UV absorption (~240 nm) band resulting from oxygen deficiencies in the chemical structure of the fiber [11]. The oxygen-vacancy bond is easily broken by absorbing one UV photon at about 240 nm, or by two-photon absorption at 480 nm, and creates a GeE' centre. It has now become clear that the mechanism responsible for the original Hill gratings [3] was two-photon absorption in the

480 nm band. Irradiation with ultraviolet light bleaches the color center absorption band, thereby changing the ultraviolet absorption spectrum of the glass. Consequently, it can be presented as a result of the Kramers-Kronoig causality relationship [12]:

$$\Delta n(\lambda) = \frac{1}{2\pi^2} P \int_0^\infty \frac{\Delta \alpha(\lambda')}{1-(\lambda'/\lambda)^2} d\lambda' \tag{2.1}$$

where P is the principal part of the integral, and $\Delta\alpha$ is the net absorption change of the fiber core, the resultant refractive index of the glass also changes, which can be sensed at the wavelength far removed from the ultraviolet region extending to the visible [13] and infrared (IR) region [14]. However, the GeE' color center model does not provide the complete explanation for all experimentally supported observations, and an alternative model based on glass densification induced by photoionization of the GeO defects has been suggested [15]. Furthermore, a stress relief model was proposed by Wong et al. [16] to explain the role that hydrogen loading plays in enhancing the magnitude of the photoinduced refractive change. Although the physical processes underlying photosensitivity are not completely known, the phenomenon of glass-fiber photosensitivity has provided an efficient way of fabricating fiber Bragg grating using ultraviolet light.

2.3 Properties of Fiber Bragg Gratings

Bragg gratings have a periodic index structure in the core of an optical fiber. Light propagating in the Bragg grating is backscattered slightly by Fresnel reflection from each successive index perturbation. Normally, the amount of backscattered light is very small except when the light has a wavelength close to the Bragg wavelength, λ_B, given by:

$$\lambda_B = 2 n_{eff} \Lambda \tag{2.2}$$

where Λ is the spatial period (or pitch) of the periodic variation and n_{eff} is the effective refractive index of the fiber core. As depicted in Fig. 2.1, this mechanism of fiber Bragg grating acts as a highly wavelength-selective reflection filter with the wavelength of the peak reflectivity at λ_B.

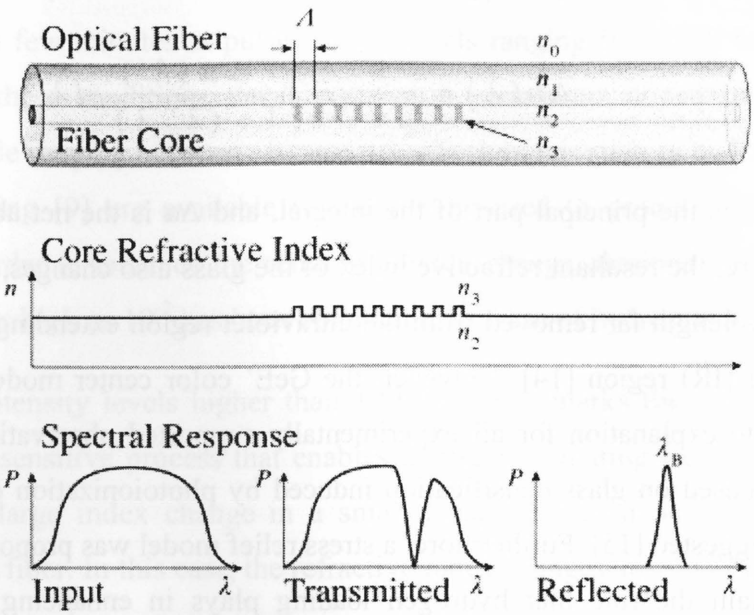

Figure 2.1 Illustration of the fiber Bragg grating properties.

Fiber Bragg gratings are produced by exposing an optical fiber to a spatially varying pattern of ultraviolet light intensity. In the most general case, we assume, for simplicity, that the index modulation $\delta n_{eff}(z)$ is a perturbation to the effective refractive index n_{eff}, that takes the form of a phase and amplitude, described by [17]:

$$\delta n_{eff}(z) = \delta n_0(z)\{1 + v \cos[\frac{2\pi z}{\Lambda} + \phi(z)]\} \tag{2.3}$$

where $\delta n_0(z)$ is the "dc" index change spatially averaged over a grating period, ν is the fringe visibility of the index change, Λ is the nominal period, and $\phi(z)$ describes grating chirp.

The optical properties of a fiber grating are essentially determined by the variation of the induced index change along the fiber axis z. Fig. 2.2 illustrates some common variations of the induced index change.

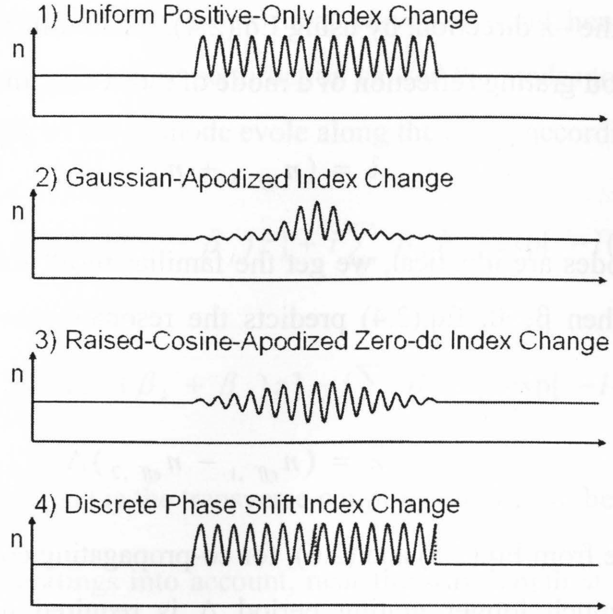

Figure 2.2 Common types of fiber gratings as classified by variation of the induced index change along the fiber axis, including 1) uniform with positive-only index change, 2) Gaussian-apodized, 3) raised-cosine-apodized with zero-dc index change, and 4) discrete phase shift (of π).

Although the grating characteristics can be understood and modeled by several approaches, coupled-mode theory [5, 18-19] is the foundametal model for the optical properties of the most fiber gratings of interest. Before we develop the quantitative analysis using coupled-mode theory, it is necessary to consider a qualitative picture of the basic interactions of interest.

Fiber gratings can be broadly classified into two types: Bragg gratings (also called reflection and short-period gratings), in which coupling occurs between modes traveling in opposite directions; and transmission gratings (also known as long-period gratings), in which the coupling is between core mode and cladding modes. Both can be described by the familiar grating equation:

$$\beta_2 = \beta_1 + m \frac{2\pi}{\Lambda} \tag{2.4}$$

where β is the mode propagation constant given by $\beta=(2\pi/\lambda)\cdot n_{eff}$. For 1st-order diffraction, which usually dominated in a fiber grating, m=-1. When $\beta_2<0$, which describe modes that propagate in the –z direction, by using Eq.(2.4), we find that the resonant wavelength for the short-period grating reflection of a mode of index $n_{eff,1}$ into a mode of index $n_{eff,2}$ is:

$$\lambda = (n_{eff,1} + n_{eff,2})\Lambda \tag{2.5}$$

If the two modes are identical, we get the familiar result for Bragg reflection condition: $\lambda=2n_{eff}\cdot\Lambda$. When $\beta_2>0$, Eq.(2.4) predicts the resonant wavelength for the long-period grating as:

$$\lambda = (n_{eff,1} - n_{eff,2})\Lambda \tag{2.6}$$

As we can see from Eq.(2.5) and (2.6), for co-propagating coupling at a given wavelength, evidently a much longer grating period Λ is required than for counter-propagating coupling. For example, in a typical single mode fiber SM28 $n_{core}=1.4468$ and $n_{clad}=1.444$, in order to obtain Bragg wavelength λ at 1500 nm, it requires $\Lambda=0.536$ μm for short-period grating and $\Lambda=535$ μm for long-period grating which is ~1000 times longer than the short-period.

In this thesis, we do not provide a derivation of couple-mode theory, as this is detailed in numerous articles and texts [20, 21]. The basic idea of the coupled-mode theory is that the electrical field of the waveguide with a perturbation can be represented by a linear combination of the modes of the field distribution without perturbation.

In the ideal-mode approximation to coupled-mode theory, it can be assumed that the transverse component of the electric field can be written as a superposition of the ideal modes labeled (i.e., the modes in an ideal waveguide with no grating perturbation), such that

$$E(x,y,z) = \sum_j [A_j(z)\exp(i\beta_j z) + B_j(z)\exp(-i\beta_j z)] \tag{2.7}$$

where $A_j(z)$ and $B_j(z)$ are slowly varying amplitude of the j^{th} mode traveling in the +z and –z direction, respectively.

While the modes are orthogonal in an ideal waveguide and hence, do not exchange energy, the presence of a dielectric perturbation caused the modes to be coupled such that the amplitude A_j and B_j of the j^{th} mode evole along the z axis according to:

$$\frac{dA_j}{dz} = i\sum_k A_k K_{kj} \exp[\, i(\beta_k - \beta_j)z] + i\sum_k B_k K_{kj} \exp[\, -i(\beta_k + \beta_j)z] \quad (2.8)$$

$$\frac{dB_j}{dz} = -i\sum_k A_k K_{kj} \exp[\, i(\beta_k + \beta_j)z] - i\sum_k B_k K_{kj} \exp[\, -i(\beta_k - \beta_j)z] \quad (2.9)$$

In Eq. (2.8) and (2.9), $K_{kj}(z)$ is the transverse coupling coefficient between modes j and k.

Take the fiber Bragg gratings into account, near the wavelength at which reflection of a mode of amplitude A(z) into an identical counter-propagating mode of amplitude B(z) is the dominant interaction in a Bragg grating. The coupled-mode equation may be simplified by retaining only terms that involve the amplitudes of the particular mode, and then making the synchronous approximation [21]. The resulting equations can be written:

$$\frac{dR}{dz} = i\sigma R(z) + i\kappa S(z) \quad (2.10)$$

$$\frac{dS}{dz} = -i\sigma S(z) - i\kappa^* R(z) \quad (2.11)$$

where the amplitude $R(z)=A(z)\exp(i\delta z-\phi/2)$ and $S(z)=B(z)\exp(-i\delta z+\phi/2)$. In the Eq. (2.10) and (2.11), κ is the "AC" coupling coefficient and σ is a general "dc" self-coupling coefficient. For a single-mode Bragg reflection grating, the κ and σ are following simple relation as:

$$\sigma = \frac{2\pi}{\lambda}\overline{\delta n_{eff}} \quad (2.12)$$

$$\kappa = \frac{\pi}{\lambda}\nu\,\overline{\delta n_{eff}} \quad (2.13)$$

where ν is the fringe visibility of the index change and ϕ describes grating chirp.

Thus, the amplitude and power reflection coefficients $\rho=S(-L/2)/R(-L/2)$ and $r=|\rho|^2$, respectively, can be described by [20, 21]:

$$\rho = \frac{-\kappa \sinh(\sqrt{\kappa^2-\sigma^2}L)}{\sigma \sinh(\sqrt{\kappa^2-\sigma^2}L) + i\sqrt{\kappa^2-\sigma^2}\cosh(\sqrt{\kappa^2-\sigma^2}L)} \tag{2.14}$$

and

$$r = \frac{\sinh^2(\sqrt{\kappa^2-\sigma^2}L)}{\cosh^2(\sqrt{\kappa^2-\sigma^2}L) - \frac{\sigma^2}{\kappa^2}} \tag{2.15}$$

The grating reflectivity, R, is given by the simple expression, $R=\tanh^2(\kappa L)$, where κ is the coupling coefficient at the Bragg wavelength and L is the length of the grating. For $\kappa L=1$, 2, 3, the grating reflectivity is 58%, 93% and 99% respectively. Fig. 2.3 shows the reflection spectra for the uniform fiber Bragg gratings when $\kappa L=1$, 3, 5, with the following parameter: $n_{eff}=1.447$, L=5000 μm, $\Delta n=0.0009$, $\Lambda=0.53559$ μm.

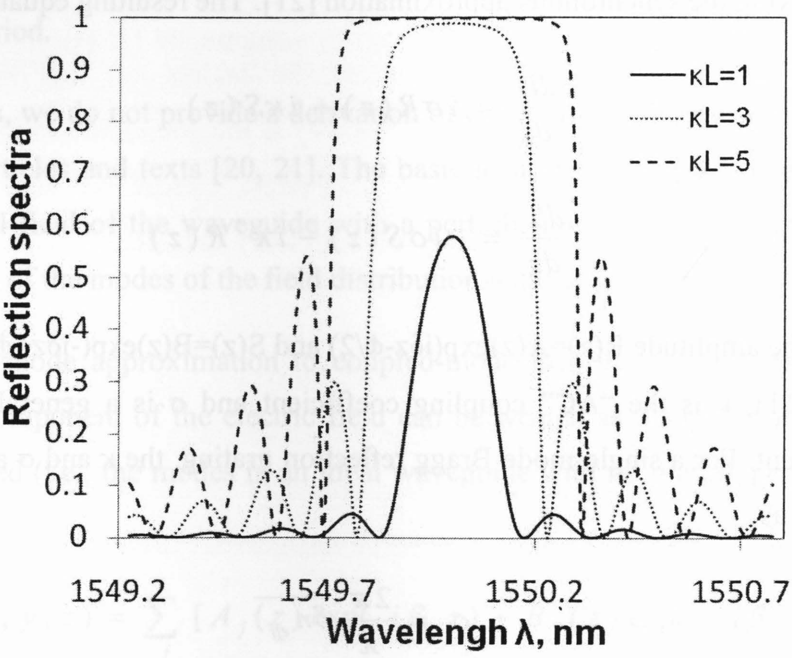

Figure 2.3 Typical reflection spectra for fiber gratings.

The other important property of the grating is its bandwidth. The bandwidth of a fiber grating that is most easily measured is its full width at half maximum (FWHM), $\Delta\lambda_{FWHM}$, which is defined as the wavelength interval between the -3dB points. This is also the point where the reflectivity has decreased to 50% of its maximum value. In the case of the weak grating ($\kappa L<<1$), $\Delta\beta_0=\beta_0-\beta_B=\pi/L$, from which it can be determined that $\Delta\lambda_{FWHM}\sim\Delta\lambda_0=\lambda_B/2n_{eff}L$. On the other hand, in the case of strong grating ($\kappa L>>1$), $\Delta\beta_0=\beta_0-\beta_B=4\ \kappa$, thus $\Delta\lambda_{FWHM}\sim2\Delta\lambda_0=4\lambda_B^2\ \kappa/\pi$.

2.4 Fabrication of Fiber Bragg Gratings

Fiber Bragg gratings can be fabricated using the holographic method [6] or the phase mask method [22, 23], illustrated in Fig. 2.4(a) and (b). The phase mask is made of a flat slab of silica glass which is transparent to ultraviolet light. On one of the flat surfaces, a one dimensional periodic surface relief structure is etched using photolithographic techniques. The shape of the periodic pattern approximates a square-shaped profile. The optical fiber is placed almost in contact with the corrugations of the phase as shown in Fig. 2.4(b). Ultraviolet light, incident normal on the phase mask, is diffracted by the periodic corrugations of the phase mask. Normally, most of the diffracted light is contained in the 0, +1, and -1 diffracted orders. However, the phase mask is designed to suppress the diffraction into the zero order by controlling the depth of the. In practice the amount of light in the zero-order can be reduced to less than 3% with approximately 80% of the total light intensity divided equally in the ±1 orders. The two ±1 diffracted beams interfere to produce a periodic pattern that photoimprints a corresponding grating in the optical fiber. If the period of the phase mask grating is Λ_{mask}, the period of the photoimprinted index grating is $\Lambda_{mask}/2$. Note that this period is independent of the wavelength of ultraviolet light irradiating on the phase mask; however, the corrugation depth required to obtain reduced zeroth-order light is a function of the wavelength and the optical dispersion of the silica.

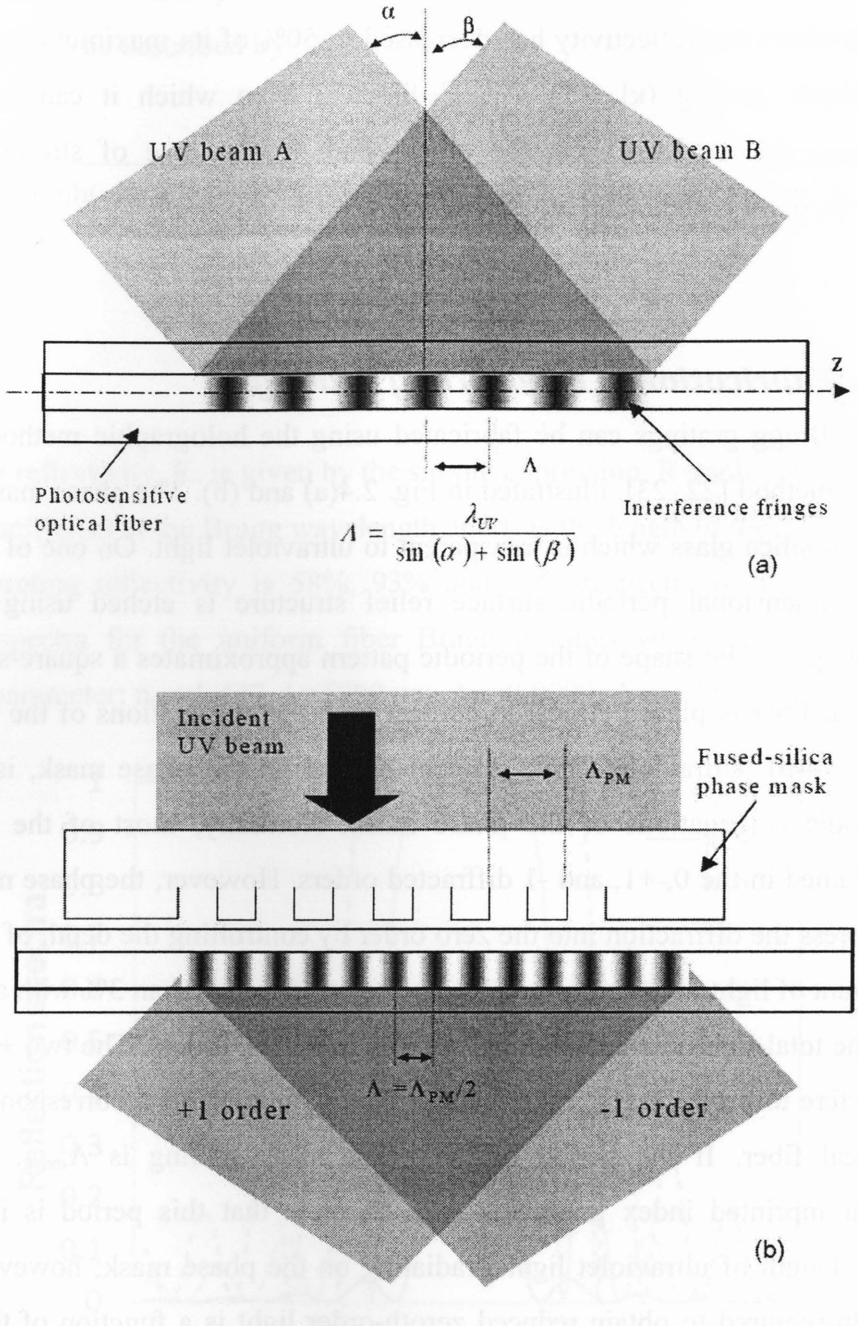

Figure 2.4 FBG fabrication techniques: (a) holographic and (b) phase mask methods.

The phase mask writing method greatly simplified the manufacturing process of Bragg gratings, and producing gratings with a high performance. In comparison with the holographic method, the phase mask technique offers easier alignment of the fiber for photoimprinting, reduces the stability requirements on the photoimprinting apparatus and coherence requirements on the ultraviolet laser beam thereby permitting the use a high power ultraviolet excimer laser source. The capability to manufacture high-performance gratings at a low cost is critical for the economic viability of using FBG in some applications. A drawback of the phase mask technique is that a separate phase mask is require for each different Bragg wavelength. However, some wavelength tuning is possible by applying tension to the fiber during the photoimprinting process; the Bragg wavelength of the relaxed fiber can be shifted as much as ~2 nm.

The phase mask technique not only yields high performance devices but is very flexible in that it can be used to fabricate gratings with controlled spectral response characteristics. For instance, the typical spectral response of a finite length grating with a uniform index modulation along the fiber length has side lobes on both sides of the main reflection peak. In applications like wavelength division multiplexing this type of response is not desirable. However, if the profile of the index modulation along the fiber length is given a bell-like functional shape, these side lobes can be suppressed [24]. The procedure is called apodization. Apodized fiber gratings have been fabricated using the phase masks technique and suppressions of the sidelobes of 30–40 dB have been achieved [25, 26].

The phase mask technique has also been extended to the fabrication of chirped fiber gratings. Chirping means varying the grating period along the length of the grating in order to broaden its spectral response. Chirped gratings are desirable for making dispersion compensators [27]. A variety of different methods have been developed to manufacture gratings that are chirped permanently [28, 29] or have an adjustable chirp [30, 31].

Another approach to grating fabrication is the point-by-point technique [32], also developed at CRC. In this method each index perturbations of the grating are written pointby-point. For gratings with many index perturbations, the method is not very efficient. However, it has been used to fabricate micro-Bragg gratings in optical fibers [33], and is most useful for making coarse gratings with pitches in the order of 100 μm for LP_{01} to LP_{11} mode conversion [32] and polarization mode conversion [5].

2.5 The applications of fiber Bragg gratings

The phase mask method, due to its inherent compatibility with optical fibers has enabled the fabrication of a variety of different FBG devices including novel devices that were not possible previously. The FBG dispersion compensator is a good example of this latter type device. FBGs have also been incorporated in optical devices simply to act as a reflector thereby transforming the device into a practical component with enhanced performance. The semiconductor laser with a pigtail containing an FBG as a wavelength locker is an example of this type of application. Although research has concentrated on the development of Bragg grating-based devices for fiber optic communications or fiber optic sensor systems, there are other potential applications in lidars, optical switching, optical signal processing, and optical storage. In the following, we list the applications that have employed fiber Bragg gratings. Only a few of the applications are described in more detail.

There are a number of potential applications for FBGs in fiber optic communications, such as dispersion compensation, wavelength selective devices, band-rejection filters of long-period gratings, fiber taps, gain-flattening in erbium-doped amplifiers, network monitoring and optical fiber identification, cascaded Raman amplification at 1.3 μm, fiber lasers and semiconductor lasers with external Bragg grating reflector. A particularly exciting application is the Bragg grating dispersion compensator. As a light pulse propagates down an optical fiber, it is dispersed, that is the width of the pulse broadens because the longer wavelength light propagaters slower than the shorter wavelength light. Consequently, at sufficiently high data rates and/or fiber lengths, the pulses in a data stream will begin to overlap. In this way, fiber dispersion limits the maximum data rate that can be transmitted through a fiber. The principle underlying the operation of the FBG dispersion compensator is as follows. A dispersed light pulse with the longer wavelengths lagging the shorter wavelengths is incident on a chirped fiber grating. The longer wavelength light is reflected near the front of the grating whereas the shorter wavelength light is reflected near the back. Thus, the short wavelengths are delayed relative to the longer wavelengths. The chirped grating can be designed so that all wavelengths in the light pulse exit the reflector at the same time and the dispersion in the optical pulse in equalized. This picture is actually too simple. In reality, the relative light pulse delay as a function of wavelength is not linear but has an oscillatory behavior [37]. However, this delay characteristic can be linearized by suitably profiling or apodizing the amplitude profile of the grating [38]. In order to make a practical device, the chirped Bragg grating must be operated in the reflection mode. This can be accomplished by incorporating the chirped grating in an optical circulator or a Mach–Zehnder (MZ) interferometer. The use of chirped Bragg gratings for dispersion compensation has been demonstrated in several laboratories [39-42].

There are several possible applications for fiber gratings that are not related to telecommunications; some of these are optical fiber mode converters such as spatial and polarization mode converters; grating-based sensors; optical signal processing such as delay line for phased array antennas; nonlinear effects in fiber Bragg gratings such as optical switching, electro-optic devices and wavelength conversion devices; and optical storage such as holographic storage, direct writing. The most promising application FBG is in the field of optical fiber sensors. In fact, the number of fiber gratings that are used in this application may exceed that of all other applications. In the following, we describe in more detail the application of FBGs as sensors.

2.6 Fiber Bragg grating sensors

The basic principle of operation commonly used in a FBG-based sensor system is to monitor the shift in wavelength of the returned "Bragg" signal with the changers in the measurand (e.g., strain, temperature, pressure and dynamic magnetic field etc.)

Most of the work on fiber Bragg grating sensors has focused on the use of the devices for providing quasi-distributed point sensing of strain and temperature. The strain response arises due to both the physical elongation of the sensor (and corresponding fractional change in grating pitch), and the change in fiber index due to photoelastic effects, whereas the thermal response arises due to the inherent thermal expansion of the fiber material and the temperature dependence of the refractive index. The shift in Bragg wavelength with strain and temperature can be expressed using [2]:

$$\frac{\Delta \lambda_B}{\lambda_B} = (1 - p_\varepsilon)\Delta \varepsilon \tag{2.11}$$

$$\frac{\Delta \lambda_B}{\lambda_B} = (\alpha + \frac{1}{n}\frac{dn}{dT})\Delta T \tag{2.12}$$

where p_ε is the photoelastic coefficient of the fibre, given by: $p_\varepsilon=(n^2/2)[P_{12}-\nu(P_{11}+P_{12})]$, where P_{ij} is the Pockel's (piezo) coefficient of the stress-optic tensor, ν is Poisson's ration, and α is the coefficient of thermal expansion (CTE) of the fiber material (e.g., silica), and ΔT is the temperature change.

In silica fiber, the photoelastic coefficient p_ε has a numerical value of ~0.22, which gives the measured strain response at constrain temperature is to be:

$$\frac{1}{\lambda_B}\frac{\Delta \lambda_B}{\Delta \varepsilon} = 0.78 \times 10^{-6}\ \mu\varepsilon^{-1} \tag{2.13}$$

The thermal response is dominated by the dn/dT effect, which account for ~95% of the observed shift. The normalized thermal responsivity at constrain strain is:

$$\frac{1}{\lambda_B}\frac{\Delta \lambda_B}{\Delta T} = 6.67 \times 10^{-6}\ C^{-1} \tag{2.14}$$

This responsivity gives a "rule-of-thumb" that in grating produced in silica fiber, representative values of the strain- and temperature-induced wavelength shifts are ~1.2 pm/με and ~10 pm/°C at 1550 nm, respectively.

The fiber Bragg gratings function as reflection devices. In order to convert the reflection spectral response into a transmission response, a Sagnac loop [44], a Michleson (or Mach-Zehnder) interferometer [45], or an optical circulator can be userd.

Compared with other implementations of fiber-optic sensors, FBG sensors have a number of distinguishing advantages. First of all, they can give an absolute measurement that is insensitive to fluctuations in the light source, as the information is usually obtained by detecting the wavelength shift $\Delta\lambda$ induced by the measurand. Moreover, unlike conventional fiber-optic interferometric sensors illuminated by highly coherent lasers, FBG sensors generally require a broadband light source and a high resolution wavelength-shift detection system.

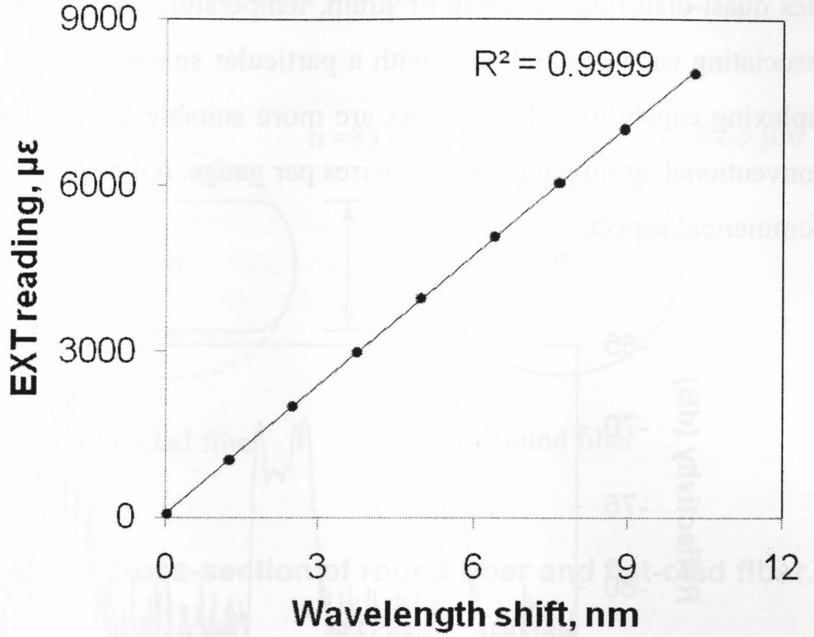

Figure 2.5 Linearity plot for peak spectrum from 0 με to 8000 με.

Secondly, the nature of the output of FBGs provides these sensors with a built-in self-referencing capability. As the sensed information is encoded directly into wavelength, which is an absolute parameter, the output does not depend directly on the total light levels, losses in the connecting fibers and couplers, or source power. Thus, it makes the FBG sensor is linear to the measurand, such as strain, temperature, pressure, etc. Fig. 2.5 shows the plot reading of strain amplitude from the extensometer against the reading of wavelength shift. It was observed that FBG sensors response was very linear to the loading, which further validates the linearity of the FBG sensors.

In addition, good physical and optical quality is widely acknowledged as one of the most important advantages of FBG sensors. The mechanical strength of an FBG produced should not be degraded significantly after fabrication. A narrow spectral bandwidth and a low excess loss (-0.2 dB to -0.3 dB) can be easily achieved, which are normally required to achieve high-resolution measurement.

Last but not least, FBG sensors facilitate wavelength division multiplexing by allowing each sensor to be assigned to a different "slice" of the available source spectrum, which enables quasi-distributed sensing of strain, temperature, or potentially other measurands by associating each spectral slice with a particular spatial location. With its outstanding multiplexing capability, FBG sensors are more suitable for localized measurement than the conventional strain gauge, with 2 wires per gauge, not only in the technical but also in the commercial aspect.

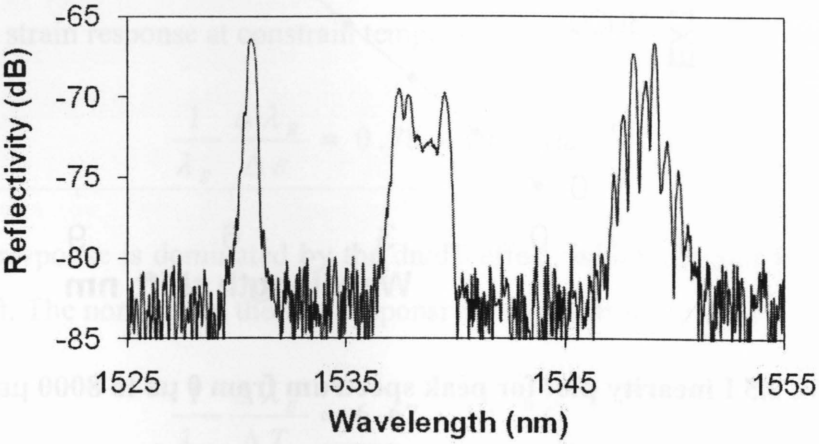

Figure 2.6 The spectra of the round FBG array at zero loads after 100 cycles at ±3000 με strain amplitude.

Electrical strain gauges are generally bonded onto a backing patch before being attached to a structure and a similar idea has been utilized for FBG applications. In order to guarantee the sensing function of FBG sensor, it is essential to ensure that the strain on the surface of the structure being monitored is able to effectively be transmitted to the sensing fiber. Whatever the precise mounting or integration technique used, it is inevitable the transfer loss occurred due to the slippage between the specimen, the adhesive and the FBG sensors at high strain levle. As shown in Fig. 2.6, only one sensor survived after strain-controlled fatigue test at strain amplitude of ±3000 με for circular-shaped FBG sensors, significantly limited the application of FBG sensors.

The material parameters (e.g., Young's modulus) and the geometry of the fiber coating are generally the parameters that affect the transfer loss. It is the goal of this study by utilizing the flat-clad fiber instead of the traditional round fiber, shown in Fig. 2.7, to increase the contact area between the FBG sensor and the surface, hence reduce the transfer loss and improve the efficiency of transmission.

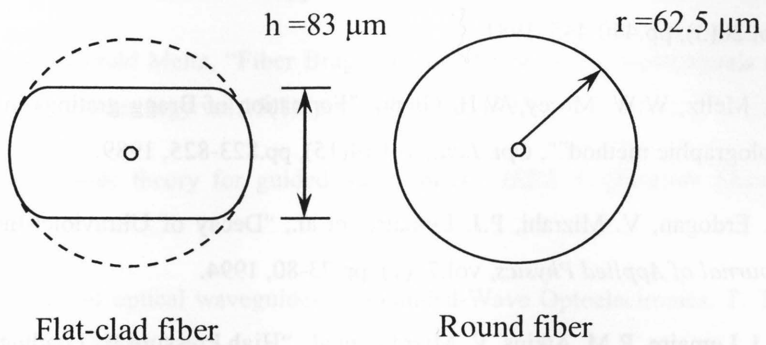

Figure 2.7 Typical cross-section of round fiber and flat-clad fiber.

Reference

1. B. Culshaw, J. Dakin, "Optical Fiber Sensors", Boston, Artech House, c1988-c1997.

2. Y.J. Rao, "In-fibre Bragg grating sensors", *Measurement Science & Technology*, vol.8(4), pp.355-375, 1997.

3. K.O. Hill, Y. Fujii, D.C. Johnson, "Photosensitivity in Optical Fiber Waveguides: Application to Reflection Filter Fabricaton", *Applied Physics Letter,* vol.32(10), pp.647-649, 1978.

4. B.S. Kawasaki, K.O. Hill, D.C. Johnson, "Narrow-Band Bragg Reflectors in Optical Fibers", *Optics Letters,* vol.3(8), pp.66-68, 1978.

5. D.K.W. Lam, B.K. Garside, "Characterization of single-mode optical fiber filters", *Appl. Opt.* vol.20(3), pp.440-445, 1981.

6. G. Meltz, W.W. Morey, W.H. Glenn, "Formation of Bragg gratings in optical fibers by a transverse holographic method"", *Opt. Lett.*, vol.14(15), pp.823-825, 1989.

7. T. Erdogan, V. Mizrahi, P.J. Lemaire, et al., "Decay of Ultraviolet-Induced Fiber Bragg Gratings", *Journal of Applied Physics,* vol.76(1), pp.73-80, 1994.

8. P.J. Lemaire, R.M. Atkins, V. Mizrahi, et al., "High Pressure H_2 Loading as a Technique for Achieving Ultrahigh UV Photosensitivity and Thermal Sensitivity in GeO_2 Doped Optical Fibers", *Electronics Letters,* vol.29(13), pp.1191-1193, 1993.

9. F. Bilodeau, B. Malo, J. Albert, et al., "Photosensitization of Optical Fiber and Silica-on-Silicon/Silica Waveguides", *Optics Letters*, vol18(12), pp.953-955, 1993.

10. K.O. Hill, F. Bilodeau, B. Malo, et al., "Birefringent Photosensitivity in Monomode Optical Fibre: Application to the External Writing of Rocking Filters", *Electronic Letters* vol.27(17), pp.1548-1550, 1991.

11. K.D. Simmons, S. Larochelle, V. Mizrahi, G.I. Stegeman, D.L. Griscom, "Correlation of defect centers with a wavelength-dependent photosensitive response in Germania-doped silica optical fibers", *Opt. Lett.*, vol.16(3), pp.141-143, 1991.

12. R. Kashyap, J.R. Armitage, R. Wyatt, S.T. Davey, D.L. Williams, "All-fiber narrow-band reflection gratings at 1500 nm", *Electron. lett.*, vol.26(11), pp.730-732, 1990.

13. D.P. Hand, P.S. Russell, "Photoinduced refractive-index changes in germanosilicate fibers", *Opt. Lett.*, vol.15(2), pp.102-104, 1990.

14. B. Malo, K.A. Vineberg, F. Bilodeau, J. Albert, D.C. Johnson, K.O. Hill, "Ultraviolet-light photosensitivity in ge-doped silica fibers - wavelength dependence of the light-induced index change", *Opt. Lett.*, vol.15(17), pp.953-955, 1990.

15. J.P. Bernardin, N.M. Lawandy, "Dynamics of the formation of Bragg gratings in germanosilicate optical fibers", *Opt. Commun.*, vol.79(3-4), pp.194-199, 1990.

16. K.S. Chiang, M.G. Sceats, D. Wong, "Ultraviolet photolytic-induced changes in optical fibers - the thermal-expansion coefficient", *Opt. Lett.*, vol.18(12), pp.965-967, 1993.

17. T. Erdogan, "Fiber Grating Spectra", *Journal of Lightwave Technology*, vol.15(8), pp.1277-1294, 1997.

18. I. Bennion, J.A.R. Williams, L. Zhang, et al., "Tutorial Review, UV-Written In-Fibre Bragg Gratings," *Optical and Quantum Electronics,* vol.28, pp.93–135, 1996.

19. Kenneth O. Hill and Gerald Meltz, "Fiber Bragg Grating Technology Fundamentals and Overview," Journal of Lightwave Technology vol.15(8), pp.1263–1276, 1997.

20. A. Yariv, "Coupled-mode theory for guided-wave optics", *IEEE J. Quantum Electron.*, vol.QE-9, pp.919-933, 1973.

21. H. Kogelnik, "Theory of optical waveguides", in Guided-Wave Optoelectronics, T. Tamir, Ed. New York: Springer-Verlag, 1990.

22. K.O. Hill, B. Malo, F. Bilodeau, D.C. Johnson, and J. Albert, "Bragg gratings fabricated in monomode photosensitive optical fiber by UV exposure through a phase mask," *Appl. Phys. Lett.*, vol.62, pp.1035–1037, 1993.

23. D.Z. Anderson, V. Mizrahi, T. Erdogan, and A.E. White, "Production of in-fiber gratings using a diffractive optical element," *Electron. Lett.*, vol.29, pp.566–568, 1993.

24. M. Matsuhara and K.O. Hill, "Optical-waveguide band-rejection filters: Design," *Appl. Opt.*, vol.13, pp.2886–2888, 1974.

25. B. Malo, S. Th´eriault, D. C. Johnson, F. Bilodeau, J. Albert, and K. O. Hill, "Apodised in-fiber Bragg grating reflectors photoimprinted using a phase mask," *Electron. Lett.*, vol.31, pp.223–224, 1995

26. J. Albert, K. O. Hill, B. Malo, S. Th´eriault, F. Bilodeau, J. D. C., and L. E. Erickson, "Apodization of the spectral response of fiber Bragg gratings using a phase mask with variable diffraction efficiency," *Electron. Lett.*, vol. 31, pp.222–223, 1995.

27. K.O. Hill, "Aperiodic distributed-parameter waveguides for integrated optics," *Appl. Opt.*, vol.13, pp.1853–1856, 1974.

28. K. Sugden, I. Bennion, A. Molony, "Chirped Gratings Produced in Photosensitive Optical Fibres by Fibre Deformation during Exposure," *Electronics Letters*, vol.30(5), pp.440–442, 1994.

29. K. C. Byron and H. N. Rourke, "Fabrication of Chirped Fibre Gratings by Novel Stretch and Write Techniques," *Electronics Letters,* vol.31(1), pp.60–61, 1995.

30. D. Garthe, R. E. Epworth, W. S. Lee, et al., "Adjustable Dispersion Equaliser for 10 and 20 Gbit/s over Distances up to 160 km," *Electronics Letters,* vol.30(25), pp.2159–2160, 1994.

31. M. M. Ohn, A. T. Alavie, R. Maaskant, et al., "Dispersion Variable Fibre Bragg Grating Using a Piezoelectric Stack," *Electronics Letters,* vol.32(21), pp.2000–2001, 1996.

32. K. O. Hill, B. Malo, K. A. Vineberg, F. Bilodeau, D. C. Johnson, and I. Skinner, "Efficient mode conversion in telecommunication fiber using externally written gratings," *Electron. Lett.*, vol.26, pp.1270– 1272, 1990.

33. B. Malo, K. O. Hill, F. Bilodeau, D. C. Johnson, and J. Albert, "Point-by-point fabrication of micro-Bragg gratings in photosensitive fiber using single excimer pulse refractive index modification techniques," *Electron. Lett.*, vol.29, pp.1668–1669, 1993.

34. A. M. Vengsarkar, P. J. Lemaire, J. B. Judkins, V. Bhatia, T. Erdogan, and J. E. Sipe, "Long-period fiber gratings as band-rejection filters," in Conf. Optic. Fiber Commun., OFC'95, San Diego, CA, 1995.

35. E. M. Dianov, V. I. Karpov, A. S. Kukov, O. I. Medvedkov, A. M. Prokhorov, V. N. Protopopov, and S. A. Vasil′ev, "Gain spectrum flattening of Erbium-doped fiber amplifier using long-period grating," in Photosensitivity and Quadratic Nonlinearity in Glass Waveguides: Fundamentals and Applications, OSA Tech. Dig. Series, vol.22, pp.14–17, 1995.

36. A. M. Vengsarkar, J. R. Pedrazzani, J. B. Judkins, P. J. Lemaire, N. S. Bergano, and C. R. Davidson, "Long-period fiber-grating-based gain equalizers," Opt. Lett., vol.21, pp.336–338, 1996.

37. K. O. Hill, F. Bilodeau, B. Malo, T. Kitagawa, S. Th′eriault, D. C. Johnson, J. Albert, and K. Takiguchi, "Aperiodic in-fiber Bragg gratings for optical fiber dispersion compensation," in Conf. Optic. Fiber Commun., OFC'94, San Jose, CA, 1994.

38. K. O. Hill, S. Th′eriault, B. Malo, F. Bilodeau, T. Kitagawa, D. C. Johnson, J. Albert, K. Takiguchi, T. Kataoka, and K. Hagimoto, "Chirped in-fiber Bragg grating dispersion compensators: Linearization of

the dispersion characteristic and demonstration of dispersion compensation in a 100 km, 10 Gbit/s optical fiber link," *Electron. Lett.*, vol.30, pp.1755–1756, 1994.

39. J. A. R. Williams, I. Bennion, K. Sugden, and N. J. Doran, "Fiber dispersion compensation using a chirped in-fire Bragg grating," *Electron. Lett.*, vol.30, pp.985–987, 1994.

40. R. Kashyap, S. V. Chernikov, P. F. McKee, and J. R. Taylor, "30 ps chromatic dispersion compensation of 400 fs pulses at 100 Gbits/s in optical fibers using an all fiber photoinduced chirped reflection grating," *Electron. Lett.*, vol.30, pp.1078–1080, 1994.

41. K. O. Hill, F. Bilodeau, B. Malo, T. Kitagawa, S. Th´eriault, D. C. Johnson, J. Albert, and K. Takiguchi, "Chirped in-fiber Bragg grating for compensation of optical-fiber dispersion," *Opt. Lett.*, vol.19, pp.1314–1316, 1994.

42. K. O. Hill, B. Malo, F. Bilodeau, S. Th´eriault, D. C. Johnson, and J. Albert, "Variable-spectral-response optical waveguide Bragg grating filters for optical signal processing," *Opt. Lett.*, vol.20, pp.1438–1440, 1995.

43. A.D. Kersey, M.A. Davis, H.J. Patrick, "Fiber Grating Sensors" *Journal of Lightwave Technology,* vol.15(8), pp.1442-1463, 1997.

44. K. O. Hill, D. C. Johnson, F. Bilodeau, et al., "Narrow-Bandwidth Optical Waveguide Transmission Filters: A New Design Concept and Applications to Optical Fibre Communications," *Electronics Letters,* vol.23(9), pp.465–466, 1987.

45. D. C. Johnson, K. O. Hill, F. Bilodeau, "New Design Concept for a Narrowband Wavelength-Selective Optical Tap and Combiner," *Electronics Letters,* vol.23(13), pp.668–669, 1987.

3 Fatigue of Metals

3.1 Introduction

The failure of a metal because of repeated loads was first documented by Albert in 1838 [1]. Since that time, considerable attention has been paid to the deformation behavior of metals under variety of loading conditions. Initially, it was recognized that a metal subjected to a repetitive or fluctuation stress will fail at a stress much lower than that required to cause fracture on a single application of load possibly by Wöhler in 1860 [2]. Failures occurring under conditions of dynamic loading are termed fatigue failures. The history of fatigue research covering a time span from 1837 to 1994 was reviewed in an extensive paper by Walter Schütz [3]. Collections of historical milestone papers were also published [4, 5]. John Mann [6] compiled 21,075 literature sources about fatigue problems covering the period from 1838 to 1969 in four books with an index on subjects, authors and years. Since then the number of publications on fatigue has still increased considerable. Fatigue failure has become progressively more prevalent as technology has developed a greater amount of equipment, such as automobiles, aircraft, compressor, pumps, turbines, etc., subject to repeated loading and vibration, until today it is often stated that fatigue accounts for at least 90% of all service failures [7].

A fatigue failure is particularly insidious because it occurs without any obvious warning. Fatigue results in a brittle-appearing fracture, with no gross deformation at the fracture. On a macroscopic scale the fracture surface is usually normal to the direction of the principal tensile stress. A fatigue failure can usually be recognized from the appearance of the fracture surface, which shows a smooth region, due to the rubbing action as the crack propagated through the section, and a rough region, where the member has failed in a ductile manner when the cross section was no longer able to carry the load. Frequently the progress of the fracture is indicated by a series of rings or "beach marks", progressing inward from the point of initiation of the failure. Another characteristic of fatigue, is that a failure usually occurs at a point of stress concentration such as a sharp corner or notch or at a metallurgical stress concentration like an inclusion.

Fatigue mechanism can be described as a phenomenon that, under a cyclic load, a fatigue crack nucleus is initiated on a microscopic scale, followed by crack growth to a macroscopic size, and finally fatigue failure in the last cycle of the fatigue life.

There are three basic factors necessary to cause fatigue failures: a tensile stress with sufficiently high value, a large enough variation in the applied stress and a sufficiently large number of cycles of the applied stress, respectively. In addition, other variables, such as stress concentration, corrosion, temperature, overload, metallurgical structure, residual stress and combined stresses, are also important element to alter the condition for fatigue. Although there are two characteristic deformations – sliding and twinning, the reason underlying the fatigue in metals is very complicated and not completely known, it is helpful to understand the fatigue behaviors and properties for considering these factors and conditions.

This chapter reviews cyclic stress-strain curve, properties of low-cycle fatigue (LCF), twinning and detwinning behavior and Vickers hardness test.

3.2 Cyclic stress-strain curve

The load amplitude is considered to be characteristic for the cyclic fatigue. A cyclic fatigue load in the present chapter is assumed to be associated with so-called constant-amplitude loading, which, in general, under conditions of stress controlled (as in the rotating-bending or cantilever-bending type of test) or strain controlled.

In actual engineering structures, stress-strain gradients do exist, and there is usually a certain degree of structural constraint of the material at critical locations. Such a condition is most reminiscent of strain control. Therefore, it is more advantageous to characterize material response under strain-controlled conditions than under stress-controlled.

Cyclic strain controlled fatigue, as opposed to the cyclic stress controlled fatigue, occurs when the strain amplitude is held constant during cycling. Strain controlled cyclic loading is found in thermal cycling, where a component expands and contracts in response to fluctuations in the operating temperature, or in reversed bending between fixed displacement. In a more general view, the localized plastic strain a notch subjected to either cyclic stress or strain condition result in strain controlled condition near the root of the notch due to the constraint effect of the larger surrounding mass of essentially elastically deformed material.

Fig. 3.1 illustrates a stress-strain loop under controlled constant strain cycling. During initial loading the stress-strain curve is O-A-B. On unloading in compression yields a lower stress C is due to the Bauschinger effect (which is that the lowering of yield stress when deformation in one direction is followed by deformation in the opposite direction). In reloading in tension a hysteresis loop develops. The dimensions of the hysteresis loop are described by its width $\Delta\varepsilon$, the total strain ranger, and its height $\Delta\sigma$, the stress range. The total strain $\Delta\varepsilon$ consists of the elastic strain component $\Delta\varepsilon_e = \Delta\sigma/E$ plus the plastic strain component $\Delta\varepsilon_p$. The width of the hysteresis loop depends on the level of cyclic strain.

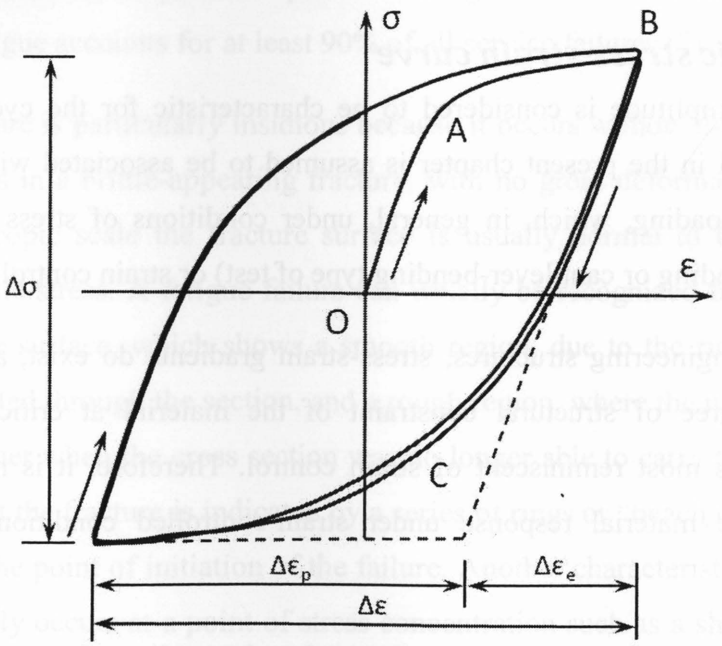

Figure 3.1 Typical stress-strain loop for constant strain cycling.

Since plastic deformation is not completely reversible, modifications to the microscopic structure of the material occur during cyclic straining and these can result in changes in the stress-strain response. Depending on the initial state a metal may undergo cyclic hardening, cyclic softening, or remain cyclically stable. It is not uncommon for all three behaviors to occur in a given material depending on the initial state of the material and the test conditions. As illustrated in Fig. 3.2, if the stress required to enforce the strain increases on subsequent reversals, the metal undergoes cyclic hardening. The hardness, yield, and ultimate strength increase. Such behavior is characteristic of annealed pure metals (for example, copper), many aluminum alloys, and as-quenched (untempered) steels.

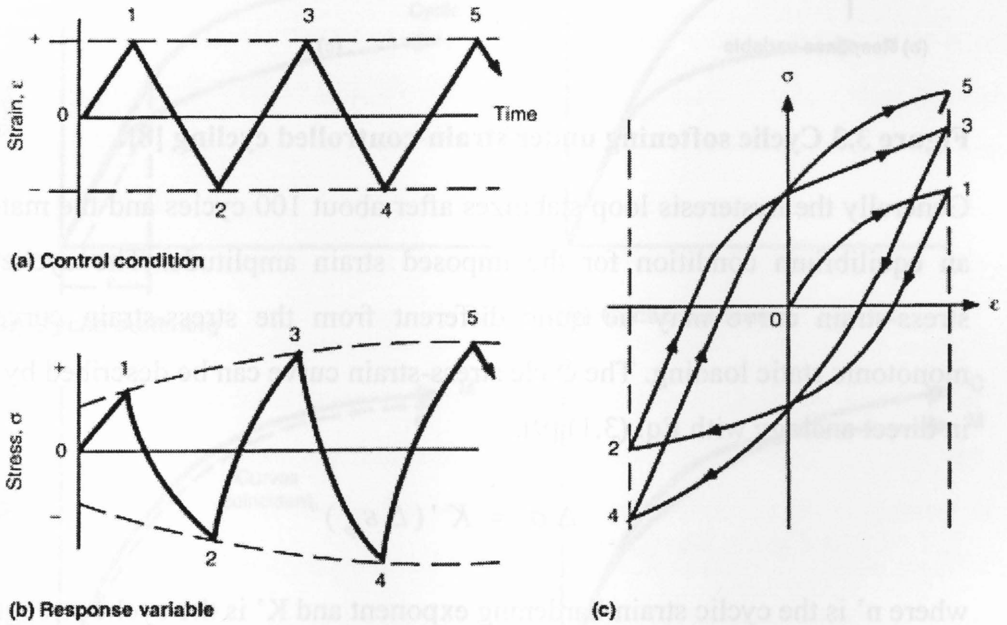

Figure 3.2 Cyclic hardening under strain-controlled cycling [8].

As illustrated in Fig. 3.3, the strain amplitude is controlled, but the stress required to enforce the strain decreases with subsequent reversals. This phenomenon is called cyclic softening. It is characteristic of cold worked pure metals and many steels at small strain amplitudes. During cyclic softening, the flow properties (for example, hardness, yield strength, and ultimate strength) decrease.

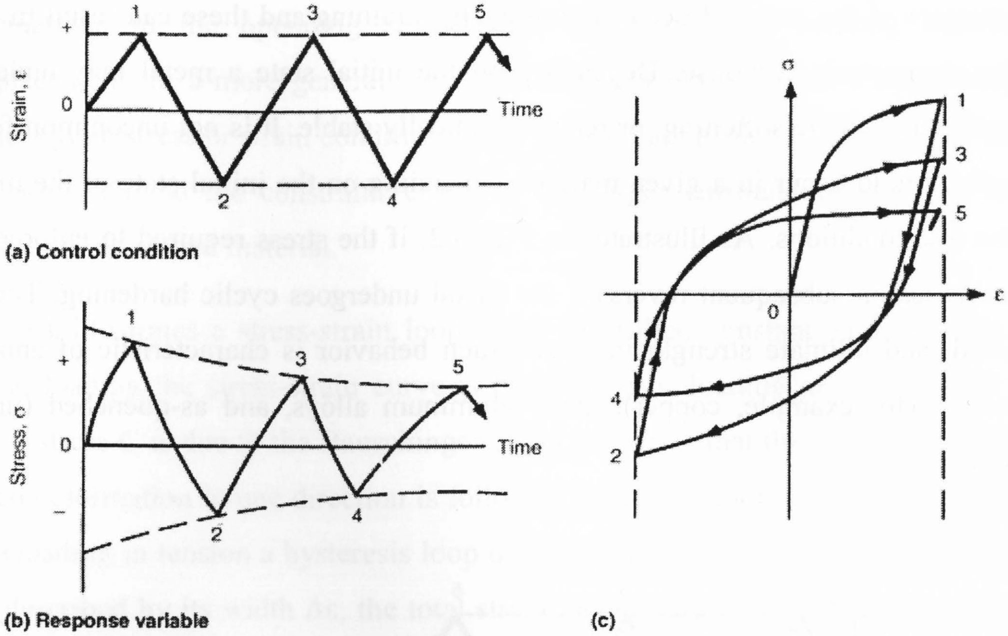

Figure 3.3 Cyclic softening under strain-controlled cycling [8].

Generally the hysteresis loop stabilizes after about 100 cycles and the material arrives at an equilibrium condition for the imposed strain amplitude. The cyclically stabilized stress-strain curve may be quite different from the stress-strain curve obtained on monotonic static loading. The cycle stress-strain curve can be described by a power curve in direct analogy with Eq. (3.1) [9].

$$\Delta \sigma = K'(\Delta \varepsilon_p)^{n'} \tag{3.1}$$

where n' is the cyclic strain-hardening exponent and K' is the cyclic strength coefficient.

Since

$$\Delta \varepsilon = \Delta \varepsilon_e + \Delta \varepsilon_p \tag{3.2}$$

and

$$\Delta \varepsilon_e = \Delta \sigma / E \tag{3.3}$$

The equation for the cyclic stress-strain curve can be express as:

$$\Delta\varepsilon = \frac{\Delta\sigma}{E} + \left(\frac{\Delta\sigma}{K'}\right)^{1/n'} \tag{3.4}$$

Eq. (3.4) describes the relationship between the stress σ and strain ε. The cyclic stress-strain curve also demonstrates the behavior of the material after it has been plastically deformed. This behavior is usually different than the initial behavior that is measured in a traditional tensile test. A simple power function is fit to this curve to obtain three material properties; cyclic strength coefficient, K', cyclic strain hardening exponent, n', and elastic modulus, E.

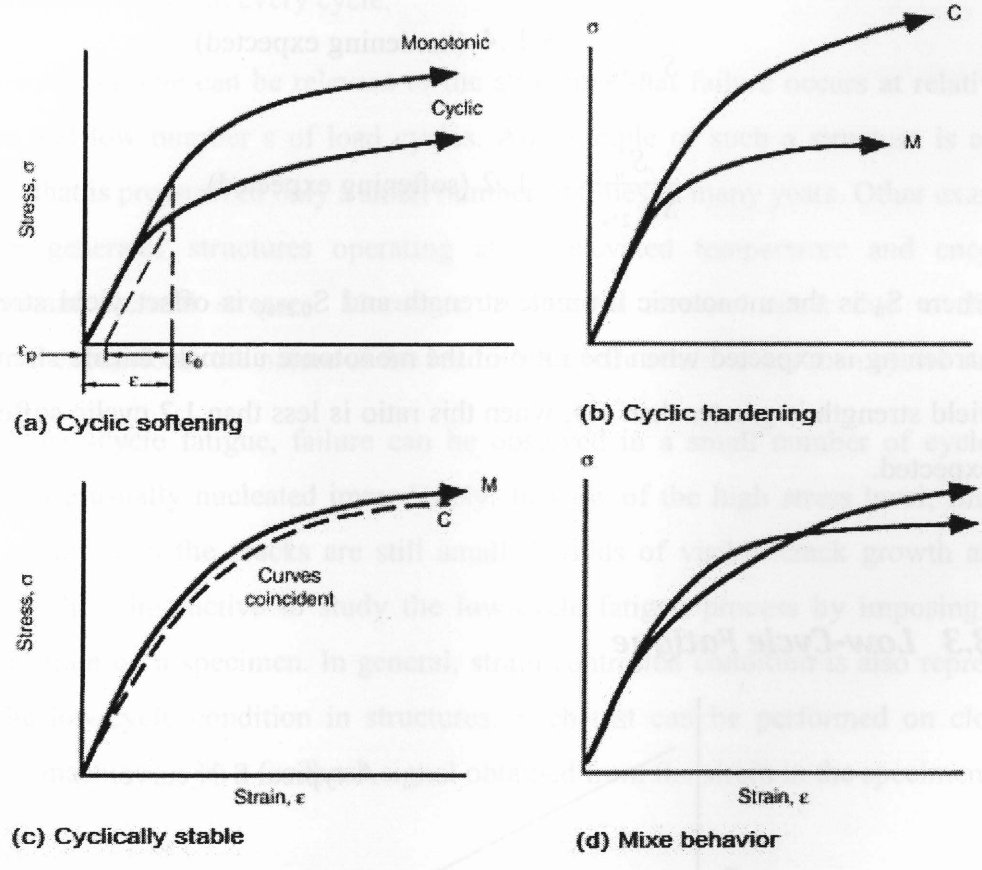

Figure 3.4 Example of various types of cyclic stress-strain curves [8].

Deformation can be observed according to the cyclic stress-strain curves, as shown in Fig. 3.4. When a material cyclically softens, the cyclic yield stress is considerably lower than the monotonic yield stress, when a material cyclically hardens, the cyclic yield stress is higher than the monotonic yield stress. Using monotonic properties in a cyclic application can result in predicting fully elastic strains, when in fact considerable plastic strains are present.

For metals n' varies between 0.10 and 0.20. In general, metals with high monotonic strain-hardening exponents (>0.15) undergo cyclic hardening; those with low strain-hardening exponents (<0.15) undergo cyclic softening.

Another method of determining what a metal will do cyclically was proposed by Smith et al. [10] and is expressed as:

$$\frac{S_u}{S_{0.2\% y}} > 1.4 \text{ (hardening expected)} \tag{3.5}$$

$$\frac{S_u}{S_{0.2\% y}} < 1.2 \text{ (softening expected)} \tag{3.6}$$

where S_u is the monotonic ultimate strength and $S_{0.2\%y}$ is offset yield strength. Cyclic hardening is expected when the ratio of the monotonic ultimate tensile strength to offset yield strength is greater than 1.4; when this ratio is less than 1.2 cyclic softening is to be expected.

3.3 Low-Cycle Fatigue

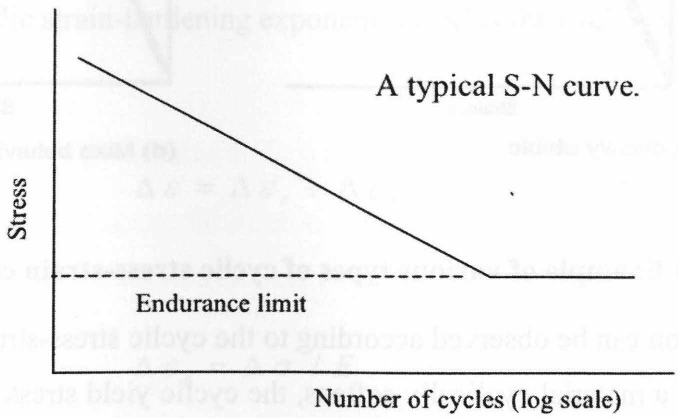

Figure 3.5 A typical S-N curve

A complete S-N (stress S against the number of cycles to failure N) curve may be divided into two portions: the low-cycle range and the high-cycle range. There is no sharp dividing line between the two. Normally we consider that low cycle is below approximately 10^4 cycles. Low-cycle fatigue as a phenomenon has received much attention since the early work of Coffin [11] and Manson [12] in the 1950s and 1960s. It became clear that low-cycle fatigue is a problem which is different from high-cycle fatigue. As pointed out before, the high-cycle fatigue mechanism on a macro scale is quasi-elastic phenomenon. However, in low-cycle fatigue, macroscopic plastic deformation occurs in every cycle.

Low-cycle fatigue can be relevant to the structures that failure occurs at relatively high stress and low number s of load cycles. An example of such a structure is a pressure vessel that is pressurized only a small number of times in many years. Other examples are power generator structures operating at an elevated temperature and encountering significant thermal stresses. Moreover, if thermal stresses occur due to differential thermal expansions, the nature of the loading is cyclic strain rather than cyclic stress [13].

Under low-cycle fatigue, failure can be observed in a small number of cycles. Small cracks are usually nucleated immediately. In view of the high stress level, final failure will occur when the cracks are still small. Periods of visible crack growth are hardly present. It is instructive to study the low-cycle fatigue process by imposing constant cyclic strain on a specimen. In general, strain controlled condition is also representative for the low-cycle condition in structures. Such test can be performed on closed-loop fatigue machines with a feedback signal obtained from the strain in the specimen.

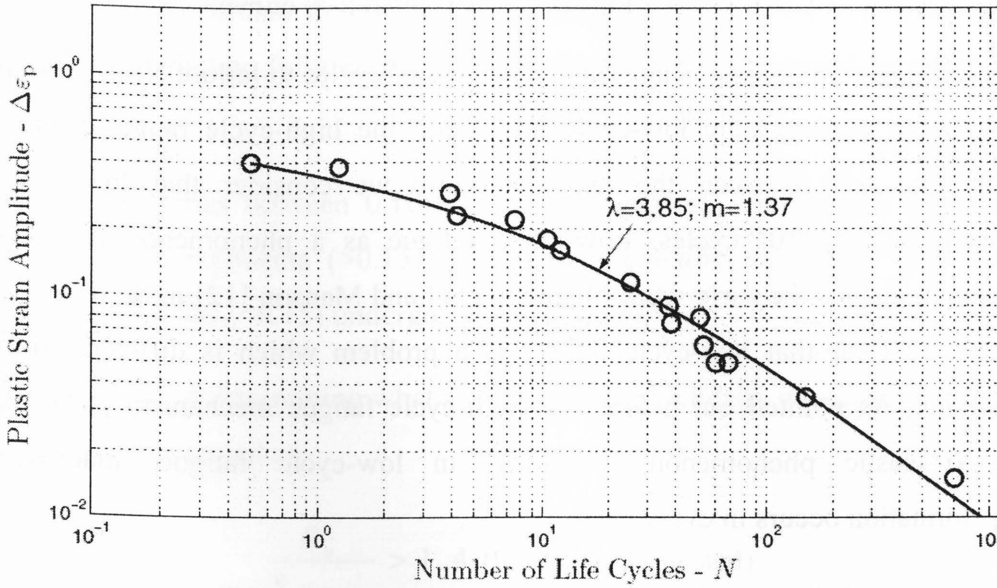

Figure 3.6 The $\Delta\varepsilon_p$-N relationship for the aluminum alloy 2024-T6. Experimental data from Coffin and Tavernelli [14].

The usual way of presenting low-cycle fatigue test result is to plot the plastic strain range $\Delta\varepsilon_p$ against N, as shown in Fig. 3.6. This type of behavior is known as the Coffin-Mason relation, which is best described by:

$$\frac{\Delta \varepsilon_p}{2} = \varepsilon_f'(2N)^c \tag{3.7}$$

where $\Delta\varepsilon_p/2$ is the plastic strain amplitude; ε_f' is the fatigue ductility coefficient defined by the strain intercept at 2N=1, which is approximately equal to the true fracture strain ε_f for many metals; 2N is the number of strain reversals to failure (one cycle is two reversals); and c is the fatigue ductility exponent, which varies between -0.5 and -0.7 for many metals.

Eq. (3.7) describes the relationship between plastic strain and fatigue life in the low-cycle fatigue regime. However, it can obviously not apply to high-cycle fatigue. For the high-cycle regime, where the nominal strains are elastic, Basquin's equation is described by:

$$\sigma_a = \frac{\Delta \varepsilon_e}{2} E = \sigma_f'(2N)^b \tag{3.8}$$

where σ_a is the alternating stress amplitude; $\Delta\varepsilon_e/2$ is the elastic strain amplitude; E is the Young's modulus; σ_f' is the fatigue ductility coefficient defined by the strain intercept at 2N=1, which is approximately equal to the monotonic true fracture strain σ_f; and b is the fatigue strength exponent, which varies between -0.05 and -0.12 for most metals.

From Eq. 3.2, an equation valid for the entire range of fatigue lives can be obtained by superposition of Eq. (3.7) and (3.8).

$$\frac{\Delta\varepsilon}{2} = \frac{\sigma_f'}{E}(2N)^b + \sigma_f'(2N)^c \tag{3.7}$$

As shown in Fig. 3.7 the fatigue strain-life curve tends toward the plastic curve at large total strain amplitude and tends toward the elastic curve at small total strain amplitudes.

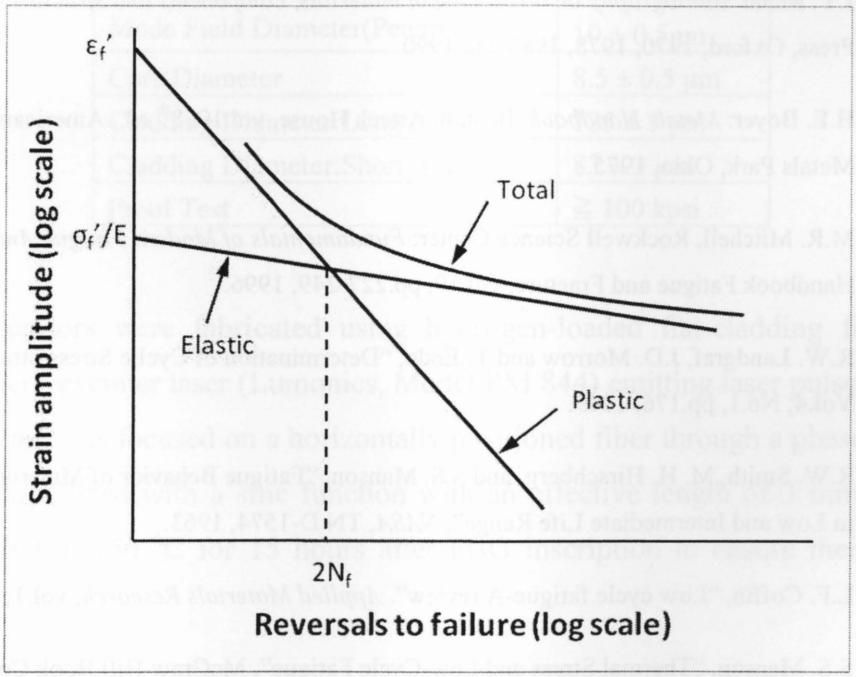

Figure 3.7 Schematic fatigue strain-life curve obtained by superposition of leastic and plastic strain-life equations

Reference

1. W.A.J. Albert, "Uber Treibseile Am Harz," *Archive Fur Mineralogie*, Geognosie, Bergbau Und Huttenkunde, vol.10, pp. 215-234, 1838 (IN GERMAN).
2. A. Wöhler, "Versuche Uber Die Festigkeit Der Eisenbahnwagenachsen," *Zeitschrift Fur Bauwesen*, vol.10, 1860 (IN GERMAN), with English Summary in Engineering, vol.4, pp.160-161, 1867.
3. W. Schütz, "A history of fatigue". *Eng. Fracture Mechanics*, vol.54, pp.263-300, 1996.
4. D. Haanewinkel and H. Zenner: *Fatigue strength. A facsimile collection of historical papers until 1950*, Technical University of Clausthal, 1989.
5. R.J. Sanfor: *Selected Papers on Foundations of Linear Elastic Fracture Mechanics*, SEM Classic papers, vol.CP1, SPIE Mileston series, vol.MS137, 1997.
6. J.Y. Mann: *Bibliography on the fatigue of materials, components and structures*, vol.1 to 4, Pergamon Press, Oxford, 1970, 1978, 1983 and 1990.
7. H.E. Boyer: *Metals Handbook*, Boston, Artech House, vol.10, 8th ed., American Society for Metals, Metals Park, Ohio, 1975.
8. M.R. Mitchell, Rockwell Science Center: *Fundamentals of Modern Fatigue Analysis for Design*, ASM Handbook Fatigue and Fracture, vol.19, pp.227-249, 1996.
9. R.W. Landgraf, J.D. Morrow and T. Endo, "Determination of Cyclic Stress-strain Curve", *J. Mater.*, Vol.4, No.1, pp.176, 1969.
10. R.W. Smith, M. H. Hirschberg, and S.S. Manson, "Fatigue Behavior of Materials under Strain Cycling in Low and Intermediate Life Range", *NASA*, TN D-1574, 1963.
11. L.F. Coffin, "Low cycle fatigue-A review". *Applied Materials Research*, vol.1, no.3, pp.129, 1962.
12. S.S. Manson, "Thermal Stress and Low-Cycle Fatigue", McGraw-Hill Book Company, New York, 1960.
13. "Manual on Low-Cycle Fatigue Testing", *ASTM Spec. Tech. Publ.* 465, 1969; "Constant Amplitude Low-Cycle Fatigue Testing", *ASTM Standard E606-80*.
14. L.F. Coffin, J. Tavernelli, "The cyclic straining and fatigue of metals", *Trans Metall Soc AIME*, vol.215, pp.794–807, 1959.

4 Experimental

4.1 Flat-clad fiber and FBG fabrication

The flat-cladding fiber (Part No: FLATCLD15, Prime Optical Fiber Corp., Taiwan, ROC) has a diameter of 125 μm and a thickness of 83 μm that provides a contact width of 93.5 μm to the substrate. The parameters of FLATCLD15 are listed in the Table 4.1.

Table. 4.1 Specifications of Flat-clad fiber

Product Name	**FLATCLD15**
Design Wavelength	1550 nm
Cut-Off Wavelength	≦ 1450 nm
Attenuation @1550nm	≦ 0.6 dB/km
Numerical Aperture	0.14 ± 0.01
Mode Field Diameter(PetermannII)	10 ± 0.5μm
Core Diameter	8.5 ± 0.5 μm
Cladding Diameter:Long Axis	125 ± 3 μm
Cladding Diameter:Short Axis	83 ± 3 μm
Proof Test	≧ 100 kpsi

The FBG sensors were fabricated using hydrogen-loaded flat-cladding fiber with a collimated KrF excimer laser (Lumonics, Model PM 844) emitting laser pulses at 248 nm. The laser beam was focused on a horizontally positioned fiber through a phase mask. The FBGs were apodized with a sinc function with an effective length of 3 mm. All FBGs were annealed at 150 ^{o}C for 15 hours after FBG inscription to ensure their long-term stability.

The FBG array had three FBG sensors at 1528.94, 1536.10 and 1543.20 nm, respectively, as shown in Fig. 4.1(b). The reflective peaks of the FBG sensors showed a high optical signal-to-noise ratio of ~30 dB. Bonding process caused the blue-shift of the FBG wavelengths by ~2 nm. However, the bandwidth and the reflectivity of each FBG remain the same.

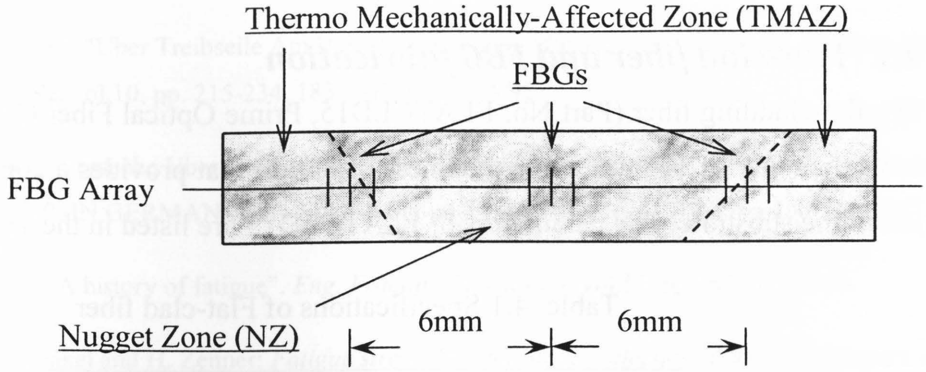

(a)

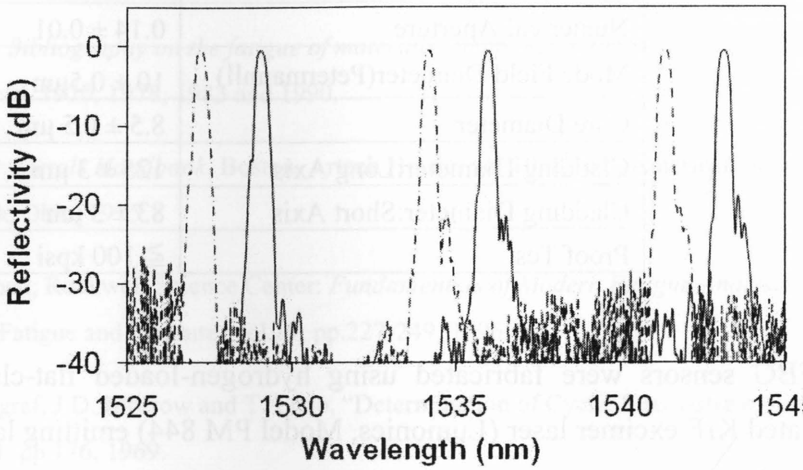

(b)

Figure 4.1 (a) Distribution of sensor in each array bonded on the side of FSWed sample; (b) Reflection spectra of a FBG sensor array before (solid line) and after (dashed line) bonded onto the aluminum base metal.

4.2 Bonding Process

To ensure that the fiber sensor was bonded to the substrate with a uniform thin layer of epoxy, the following procedure was used. A dog-bone shaped specimen was grounded with #320 and then #600 sand papers in the direction perpendicular to the long axis of the specimen. Two stripes of aluminum-tape of ~0.10 mm thick were placed alongside the fiber to form a trench of about 1.5 mm wide. After filling the trench with epoxy (353ND, EPO-TEK), a stripe of non-stick paper and then a thin rubber sheet were used to cover the trench and fiber. We placed a rectangular-shaped weight on the top of the rubber sheet to press the fiber uniformly against the substrate as shown in Fig. 4.2. The assembly was then placed in an oven for epoxy curing at 80 °C for 45 minutes.

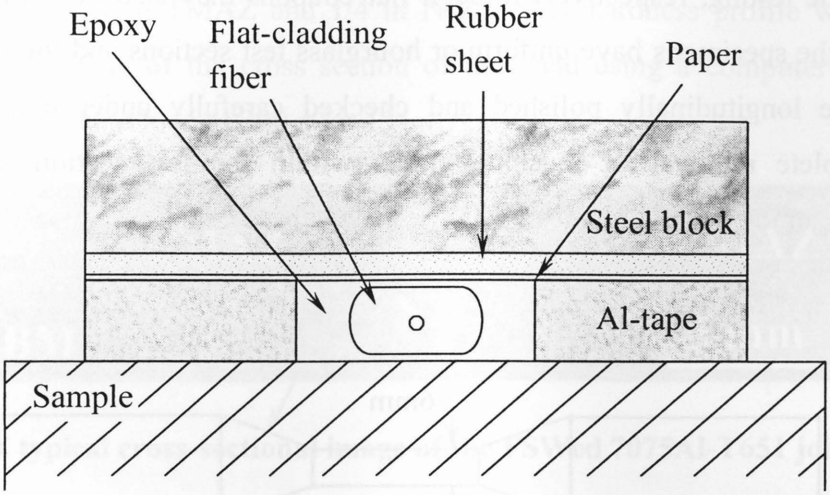

(a)

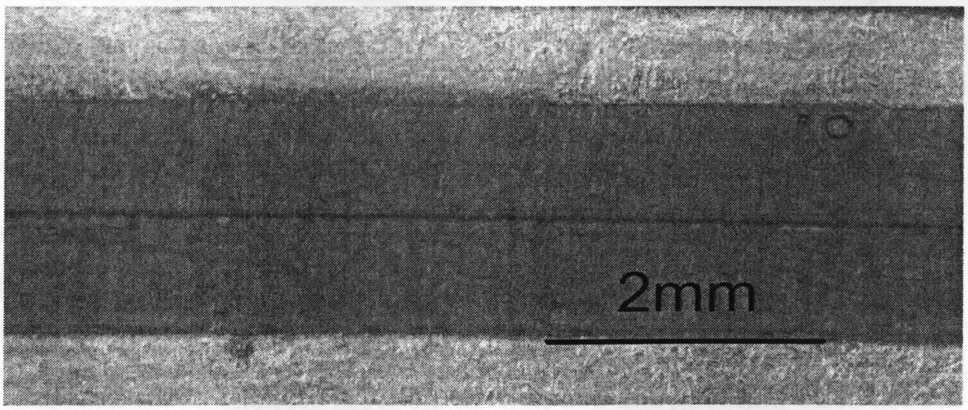

(b)

Figure 4.2 (a) Schematic diagram of the bonding process in cross section; (b) Light microscope image of a bonded FBG sensor array

4.3 Specimen fabrication

ASTM Standards E8M (ASTM, 2001) and E606 (ASTM, 1998a) list various types of sample configurations and dimensions for use in monotonic and constant-amplitude axial fatigue tests. According to the relevant standards, cylindrical specimens of approximately 12mm and 6mm diameter are normally tested for monotonic tensile and strain–life fatigue testing, respectively, though flat coupons may also be used. It is recommended that the specimens have uniform or hourglass test sections and the specimen surface has to be longitudinally polished and checked carefully under magnification to ensure complete removal of machine marks within the test section. Fig. 4.3 shows the configurations and dimensions of the fatigue test samples.

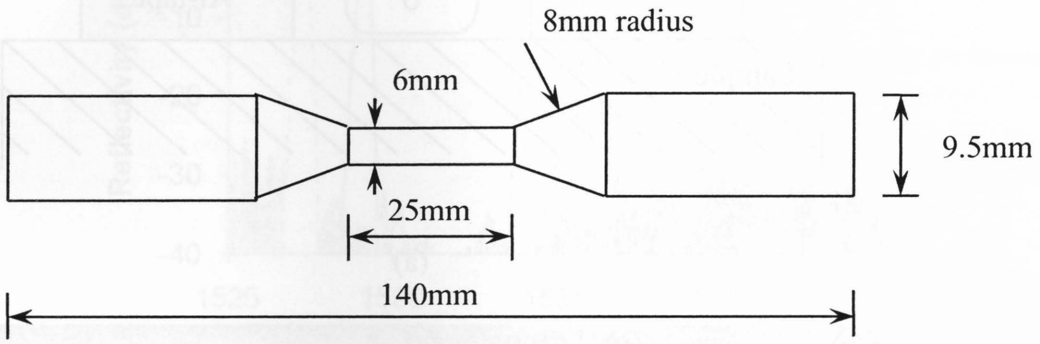

Figure 4.3 Configurations and dimensions of exemplary fatigue samples.

There were three types of specimen used in the fatigue test. The rolled aluminum alloy plates of 6.35 mm thick commercial 7075Al-T651, with a composition of 5.6Zn-2.5Mg-0.5Fe-0.16Cu-0.23Cr-0.3Mn-0.2Ti (wt.%), was used as a base metal, which had a gauge section of 25 mm long and 6×6 mm^2 in the cross-section.

The second type specimen, the friction stir welded (FSWed) sample, used the same material as the base metal, FSWed along the rolling direction using a FSW machine (China FSW Center) with a steel tool (with a shoulder of Φ20 mm and a cylindrical threaded pin of Φ8 mm). The tool rotational rate was at 1000 rpm, and the welding speed was 400 mm/min. Subsized fatigue specimens following ASTM E8 standards with a gauge section of 25 mm × 6 mm × 5.6 mm, were machined perpendicular to the FSW direction. Fig. 4.4 shows a typical cross-sectional image of the FSWed 7075Al-T651 joint where four zones, namely, nugget zone (NZ), thermo mechanically-affected zone (TMAZ), heat-affected zone (HAZ) and base metal (BM), can be seen. The FBG sensors of 3 mm long were surface mounted in the center of NZ and across the boundary between TMAZ and NZ (3/4 in TMAZ and 1/4 in NsZ). Microhardness profile was produced along the bottom line of the cross section of the weld using a computerized Buehler hardness tester under a load of 300 g for 15s.

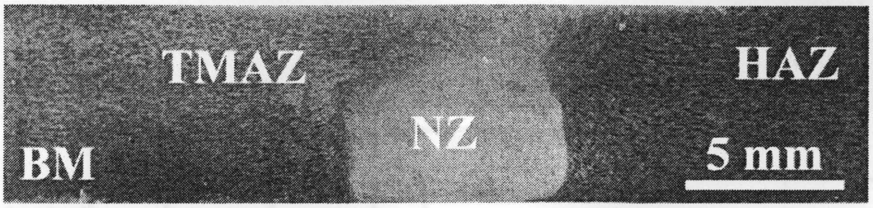

Figure 4.4 A typical cross-sectional image of the FSWed 7075Al-T651 joint

The last specimen was an extruded magnesium alloy commercial AZ31, with a composition of 3.1Al-1.05Zn-0.54Mn-0.0035Fe-0.0007Ni-0.0008Cu (wt.%). Subsized samples for fatigue tests, having a gage length of 25 mm × 6 mm × 7 mm, were extruded in a temperature range of 360-382 °C at an extrusion exit speed of 50.8 mm/s. The applied extrusion ratio was ~6, and after extrusion the alloy was air quenched.

4.4 *Strain-controlled fatigue testing system*

A commercial closed-loop servohydraulic axial load frame is used to conduct the tests. An extensometer or a high-quality clip gauge is used to measure the strain. The test system uses the strain output to provide feedback to the servocontrollers. Figure 4.5 illustrates the schematic diagram of a strain-controlled fatigue testing system layout. To protect the specimen surface from the knife edge of the extensometer, ASTM E606 recommends the use of a transparent tape or epoxy to cushion the attachment. Most of the tests are conducted at room temperature. To minimize temperature effects on the extensometer and load cell calibration, ASTM E606 requires that temperature fluctuations be maintained within ±2 °C.

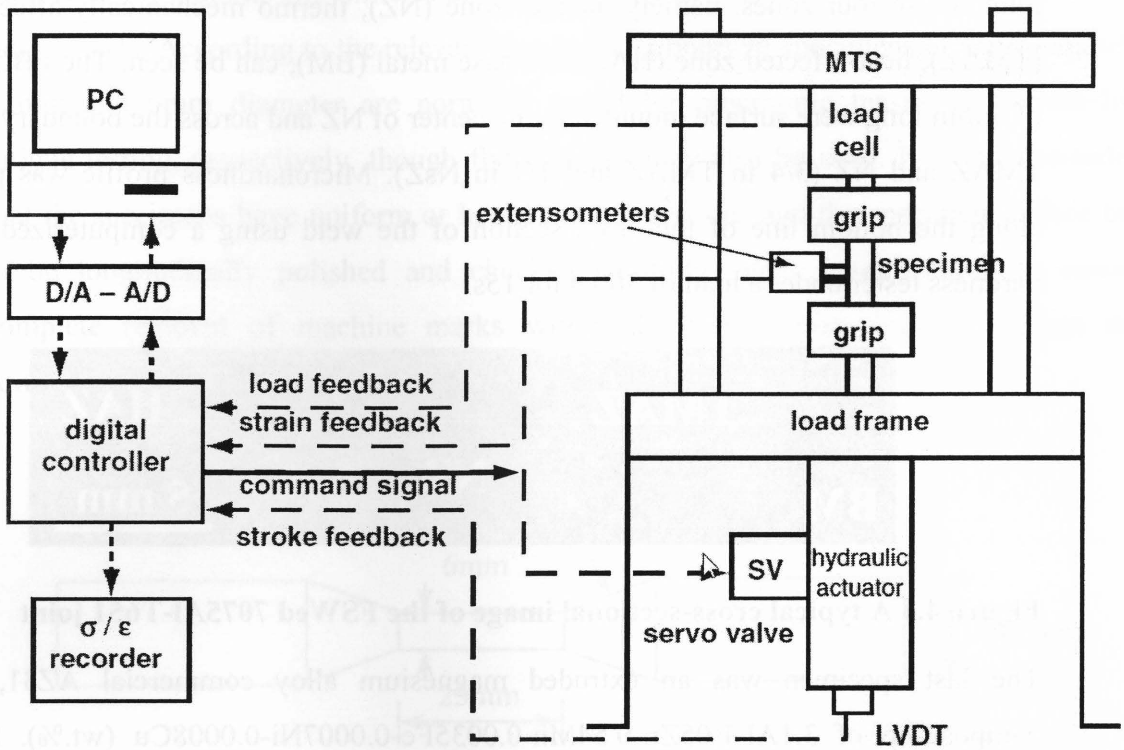

Figure 4.5 Schematic diagram of the strain-controlled fatigue testing system layout.

As shown in Fig. 4.6, strain-controlled, push-pull type fatigue tests were carried out using a computer-controlled Instron fatigue testing system (Instron FastTrack 8800, Norwood, MA). In the fatigue testing, a triangular waveform with a strain ratio of R= -1 was applied at a constant strain rate of 1×10^{-2} s^{-1}. The sample was tested for 100 cycles, starting from the cyclic strain amplitude of ±2000 με, until failure with a cyclic strain amplitude increment of ±1000 με. An extensometer of 12.5 mm or 25.0 mm in gauge length was used to measure the strain and provided feedback to the system for strain control. During the LCF tests the wavelength shifts of the FBGs were recorded by a sensor interrogation system (Model si425, Micron Optics) and then were converted into the strain by a gauge factor of 1.25 με per pm. The shift of the Bragg wavelength, λ_B with the strain, ε, can be expressed by Eq. 2.13.

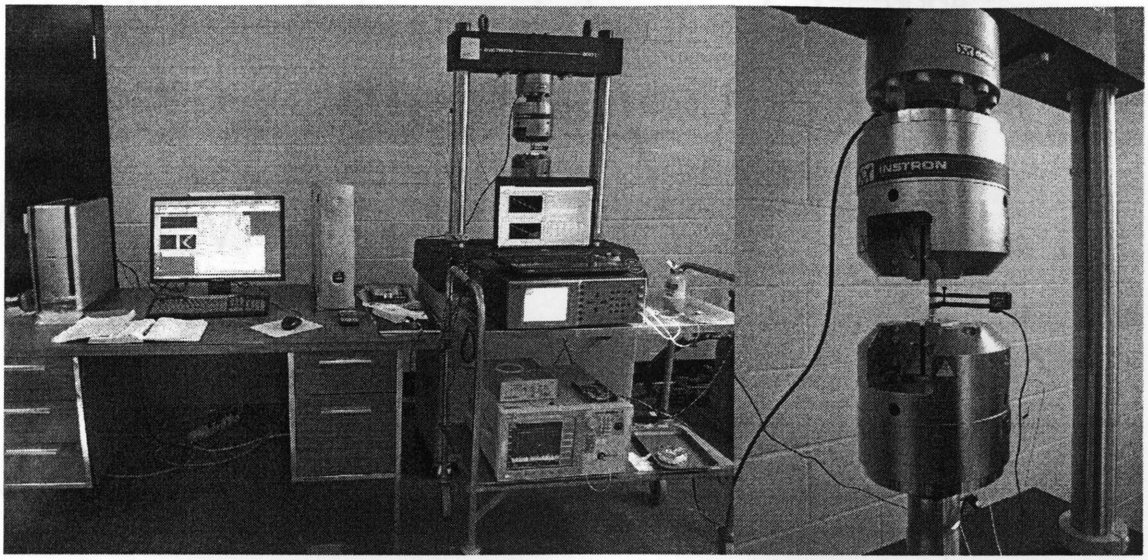

Figure 4.6 Experiment setup of the fatigue test

The applied load was recorded simultaneously from an analog output port of the Instron system using an analog-to-digital data acquisition card (Model USB-6215, National Instrument) and was converted into the stress. Thus, both strain and stress values were recorded as a function of time for each fatigue cycle, as shown in Fig. 4.7.

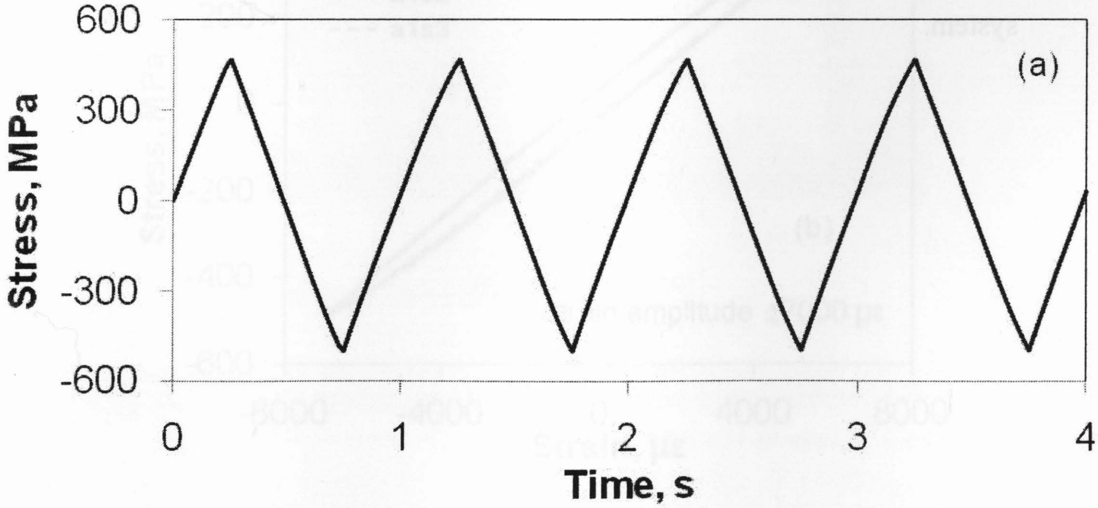

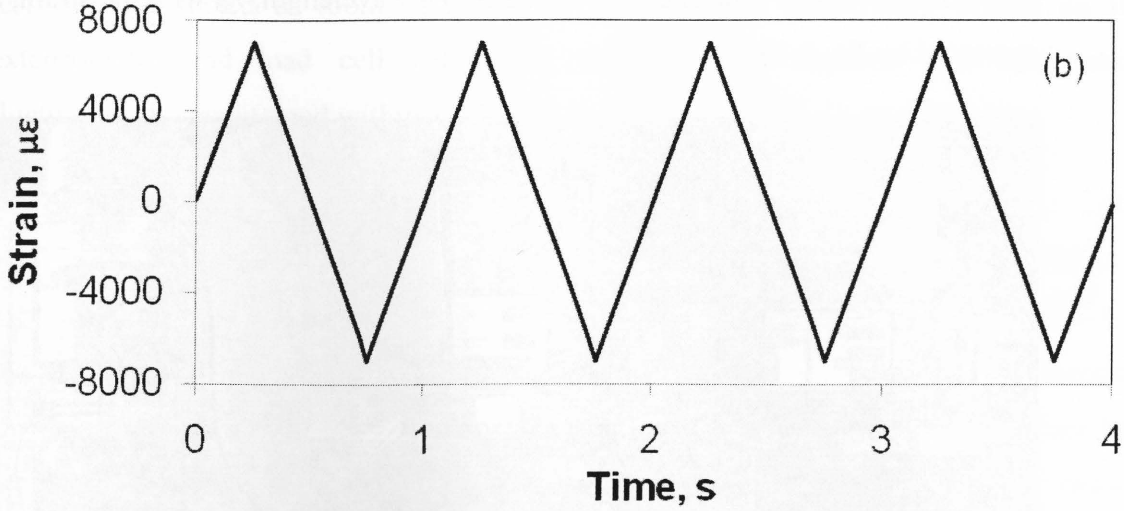

Figure 4.7 Measured stress (a) and strain (b) as a function of time of 1st-4th cycles for the base metal sample at cyclic strain amplitude of ±7000 με.

Low-cycle fatigue tests were conducted at cyclic strain amplitude of ±0.2, 0.3, 0.4, 0.5, 0.6, 0.7 and 0.8 % until sample broken. The triangular loading waveform was carried out at a zero mean strain of a frequency of 0.25 Hz. Both the interrogator Micron si425 and data acquisition card NI USB-6215 was set 1000 Sample/s synchronously, which is 5 times more precise than that of 200 data point each cycle from the Instron fatigue testing system.

5 Results and Discussions

5.1 Fatigue test of Aluminum alloy 7075Al-T651 base metel

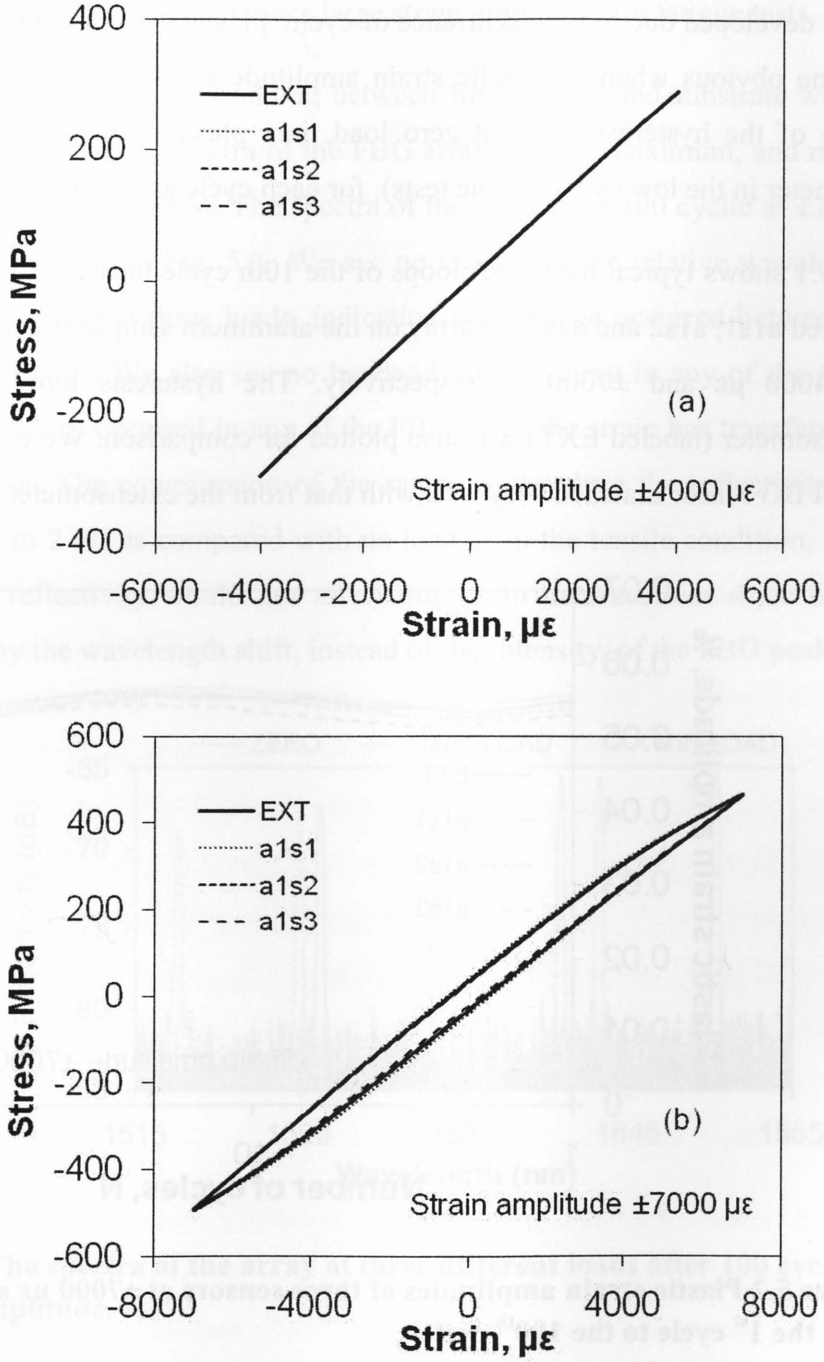

Figure 5.1 FBG sensor measured strains as a function of applied stress at the 10th cycle at (a) ±4000 με and (b) ±7000 με strain amplitude.

In the fatigue tests of below ±4000 με strain amplitude, the stress dependence on the strain was basically linear as expected, and the plot of stress versus strain curve showed a straight line. As the strain amplitude increased, a hysteresis loop of the stress versus strain developed due to the occurrence of cyclic plastic deformation. The hysteresis loops became obvious when the cyclic strain amplitude exceeded ±6000 με. I measured the width of the hysteresis loop at zero load, i.e., plastic strain amplitude (an important parameter in the low cycle fatigue tests), for each cycle as the cycling progressed.

Fig. 5.1 shows typical hysteresis loops of the 10th cycle measured by three FBG sensors (labeled a1s1, a1s2 and a1s3) in array on the aluminum sample at cyclic strain amplitudes of ±4000 με and ±7000 με respectively. The hysteresis loop measured from the extensometer (labeled EXT) was also plotted for comparison. We can see that the results from FBG sensor matched very well with that from the extensometer.

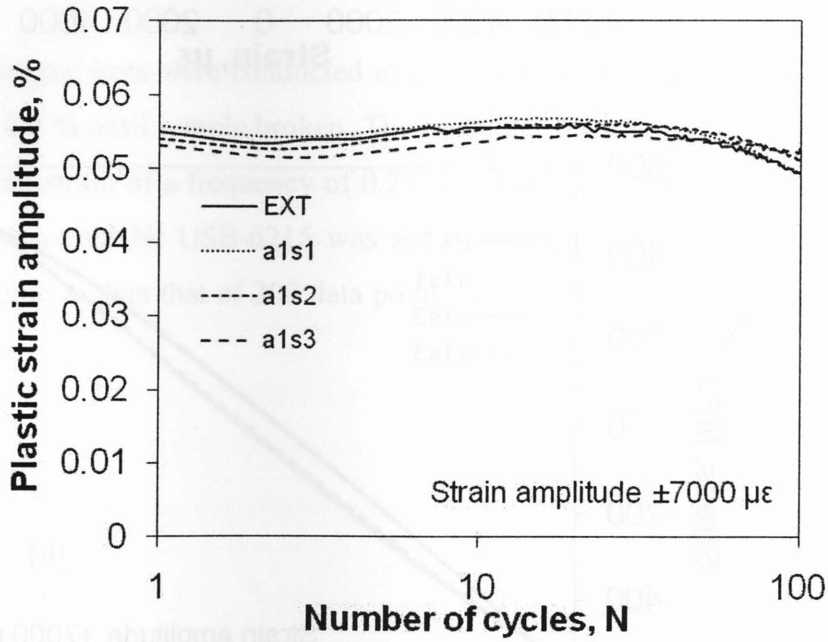

Figure 5.2 Plastic strain amplitudes of three sensors at ±7000 με strain amplitude from the 1st cycle to the 100th cycle.

We also compared the measured plastic strain amplitudes from the three FBG sensors with that from extensometer for all 100 cycles as shown in Fig. 5.2. Again good agreement was observed not only in the magnitude but also in the trend of strain variation reflecting cyclic hardening-softening behavior of materials. The largest difference in the plastic strain amplitude measured by three FBG sensors was about 30 με, which was only 0.43% of the cyclic strain amplitude of ±7000 με. This clearly validated that flat-cladding FBG sensors can be used to measure large strain amplitudes in fatigue tests.

In order to determine if the bonding between fiber sensor and substrate was still intact, we measured the optical spectra of the FBG array at zero, maximum, and minimum load after each cyclic loading test. The spectra of the array after 100 cyclic at ±7000 με strain amplitude are shown in Fig. 5.3. We see no change in the relative wavelength spacing between the sensors at three loads, indicating no slippage occurred between the sample and optical sensors. We also see no bandwidth broadening in any of the three sensors, indicating no chirp occurred in any of the FBGs, i.e., the strain has transferred uniformly along the fiber. The compression of the sample did reduce the reflectivity of the FBG sensors by 1 to 2 dB as compared with no load or in the tensile condition. Nevertheless, the reduced reflectivity would not affect our strain measurement since the strain was determined by the wavelength shift, instead of the intensity, of the FBG peak,

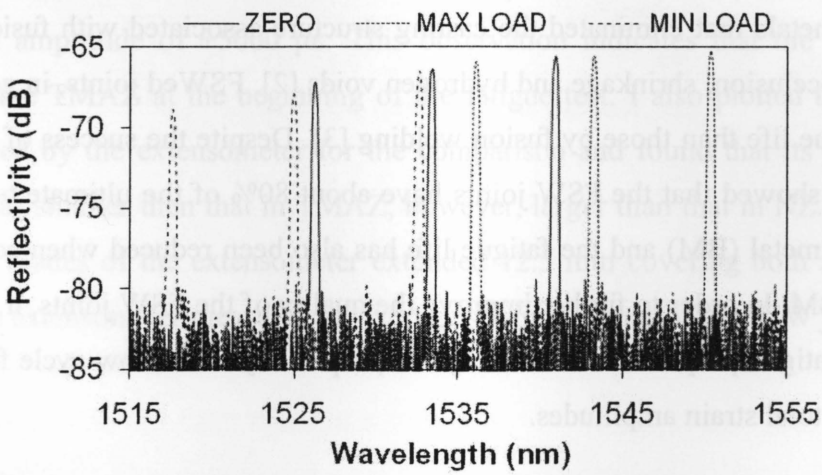

Figure 5.3 The spectra of the array at three different loads after 100 cycles at ±7000 με strain amplitude.

We also tested the same sample at cyclic strain amplitudes of ±8000 με for 100 cycles. The measured plastic strain amplitudes from the three FBGs agreed with that from the extensometer as well. However, the largest difference in the plastic strain amplitudes from three FBG sensors increased to ~150 με, i.e., 1.9% of the strain amplitude at ±8000 με. Also observed was the slightly bandwidth broadening of the FBG peaks under compression after 100 cycling. The bandwidth broadening indicated that strain transfers started to become non-uniform along the fiber as the strain amplitude increased to ±8000 με. The aluminum sample broke at the 9th cycle in the ±9000 με strain amplitude tests. Based on these data, we can conclude that the upper limit of the strain measurements using the flat-cladding FBG sensor was around ±8000 με for this base metal. This limit could be further extended by the improvement of bonding material and process, such as using the epoxy with high shear modulus.

5.2 Fatigue test of FSWed Aluminum alloy 7075Al-T651

Friction stir welding (FSW), developed at The Welding Institute (TWI) of United Kingdom in 1991 [1], had offered an innovative solution to the joining of some difficult-to-weld materials. FSW has many advantages compared with conventional fusion welding [2-4]. In FSW process, the temperature is kept much below the melting point of the metals that eliminated the casting structure associated with fusion welding, such as: gas occlusion, shrinkage and hydrogen voids [2]. FSWed joints, in general, have a longer fatigue life than those by fusion welding [3]. Despite the success of the FSW, the tensile tests showed that the FSW joints have about 80% of the ultimate tensile strength of the base metal (BM) and the fatigue life has also been reduced when compared with that of the BM. In order to further improve the quality of the FSW joints, it is necessary to study the fatigue properties of FSWed joints, especially in the low cycle fatigue (LCF) tests at high total strain amplitudes.

FSWed joints fractured often at the boundary between TMAZ and HAZ. The microstructural examinations and hardness tests revealed significant difference in grain sizes and hardness values in NZ and in TMAZ, respectively [5,6]. The non-uniformity across the FSWed joints would be expected to result in different deformation characteristics. It is thus of great interest to identify the deformation characteristics in these zones separately in order to understand the failure mechanism. However, the conventional thin-film strain gauge cannot be used to measure large strains during cyclic deformation; and the extensometer, while being capable of gauging large strain amplitudes, is relatively large in size, so it only measures averaged strain over its gauge length.

For the measurement of the fatigue properties in the different zones of the aluminum alloy FSW joint, a FBG array with 3 FBG sensors was bonded on the back surface of the sample. The middle sensor was placed at the center of the NZ, the other two sensors were bonded across the boundary of the NZ and TMAZ (3/4 in TMAZ and 1/4 in NZ) symmetrically to the center. The fatigue tests were conducted with the same parameters as those for the base metal. It was observed the plastic deformation staring at low strain amplitude of ±4000 με and the deformation increased with the increase of strain amplitude. As the strain amplitudes increased to ±5000 με, very different hysteresis loops were observed in NZ and TMAZ. The plastic strain amplitude was much smaller in NZ as shown in Fig. 5.4(a) when compared with that in TMAZ shown in Fig. 5.4(b). The hysteresis loops measured from two sensors located mostly in TMAZ were very close to each other with the maximum difference of the loop's width of ~66 με, i.e., 1.3% of the cyclic strain amplitude of ±5000 με. This observation indicates that the NZ is much harder than the TMAZ at the beginning of the fatigue test. I also plotted the hysteresis loop measured by the extensometer for the comparison and found that its plastic strain amplitude was smaller then that in TMAZ, however, larger than that in NZ. Considering that the two blades of the extensometer extended 12.5 mm covering both zones, it was clear that the extensometer measured an average strain response of the FSW joint.

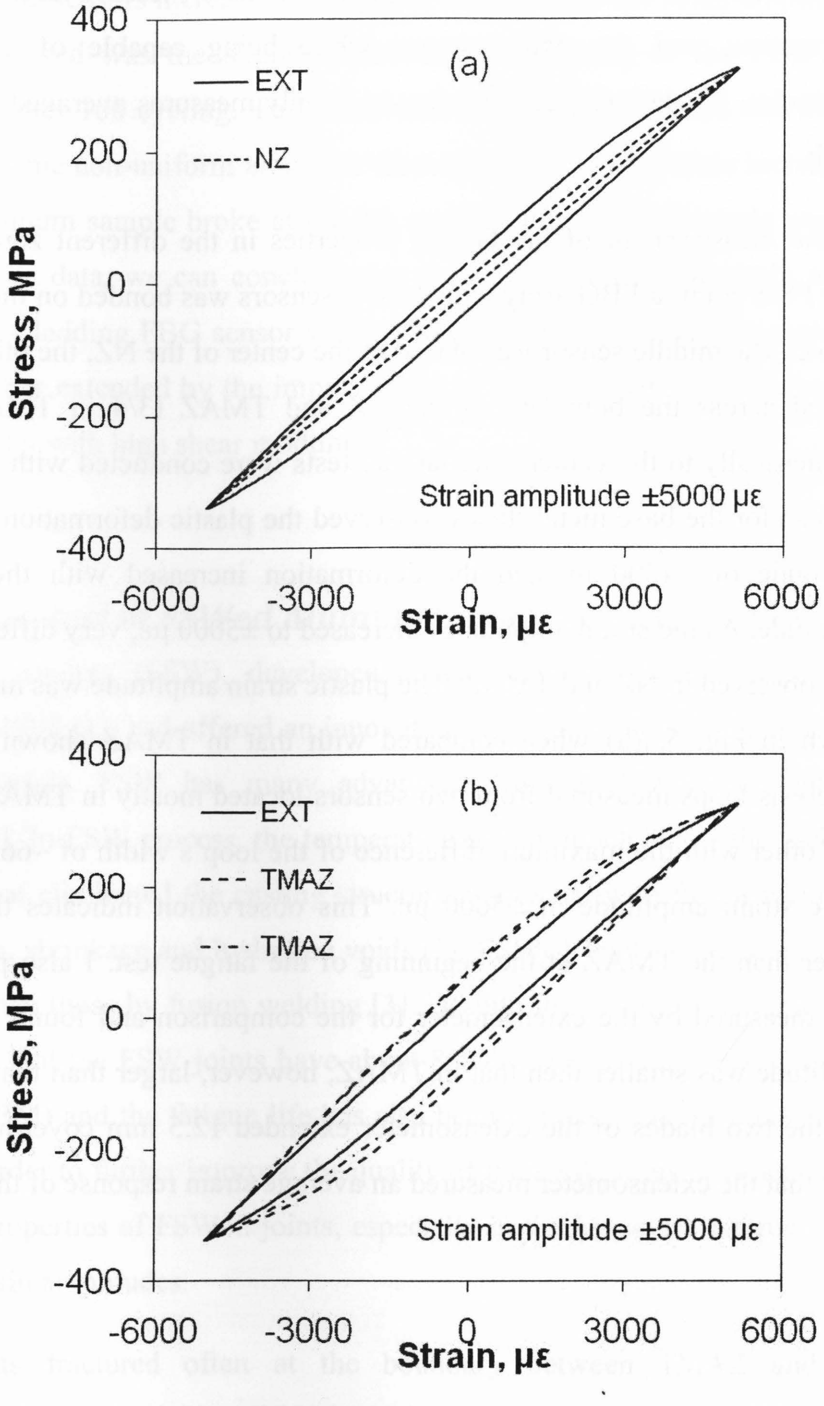

Figure 5.4 Hysteresis loops measured by FBG sensors at the 10th cycle at ±5000 με strain amplitude; (a) in NZ, and (b) in TMAZ.

The width of the hysteresis loops in NZ and TMAZ zones could be well correlated with the hardness profile, as shown in Fig. 5.5, where a significant decrease in the hardness from HV 150 in the NZ to HV 135 at the boundary between TMAZ and HAZ was observed. The hardness of the BM was measured to be about HV 165. This measurement confirmed that the NZ was harder than the TMAZ at the beginning of fatigue cycling. Since the difference in the cyclic deformation behavior in the NZ and TMAZ would directly affect the fatigue lifetime of the FSWed joints, the FBG measurements could provide valuable information towards the improvement of FSW process.

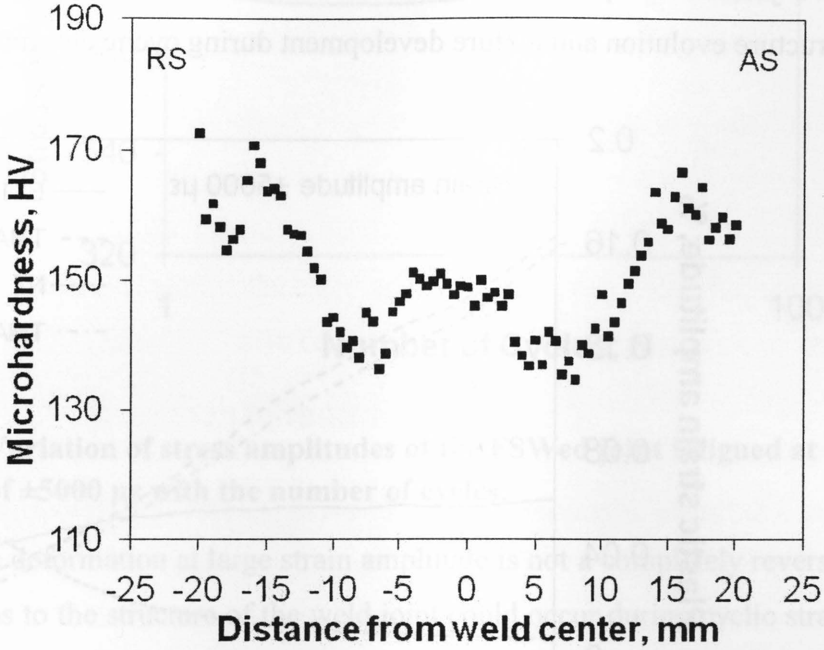

Figure 5.5 Vickers micro-hardness profiles across the FSW joint at the bottom surface.

The measured plastic strain amplitudes from the three FBG sensors with that of extensometer was further compared for all 100 cycles (Fig. 5.6). A remarkable difference in the fatigue properties of the two zones was observed. In the TMAZ, the plastic strain amplitude decreased from 0.16% at the 1st cycle monotonically to 0.024% at 100th cycle, while in the NZ it increased gradually from ~0.01% at the 1st cycle, reached the maximum of 0.053% at ~80th cycle, then slightly decreased towards the 100th cycle. These results indicated that cyclic softening occurred in the initial harder NZ, while cyclic hardening appeared in the initial softer TMAZ. The observations were in agreement with that the occurrence of cyclic hardening or softening was dependent on the initial state of the test material. In the recrystallized soft state cyclic hardening occurred, while in the hardened state cyclic softening ensued. In comparison with the NZ, the TMAZ (or the TMAZ-HAZ boundary) had a lower hardness value (Fig. 5.5), thus cyclic hardening would be expected to occur. While the cyclic hardening or softening in different zones could be generally understood from the hardness variation, this study represented only an initial exploration of localized cyclic deformation behavior of FWSed joints via optical fiber sensors. Further detailed studies on the dislocation substructure evolution and texture development during cyclic deformation are needed.

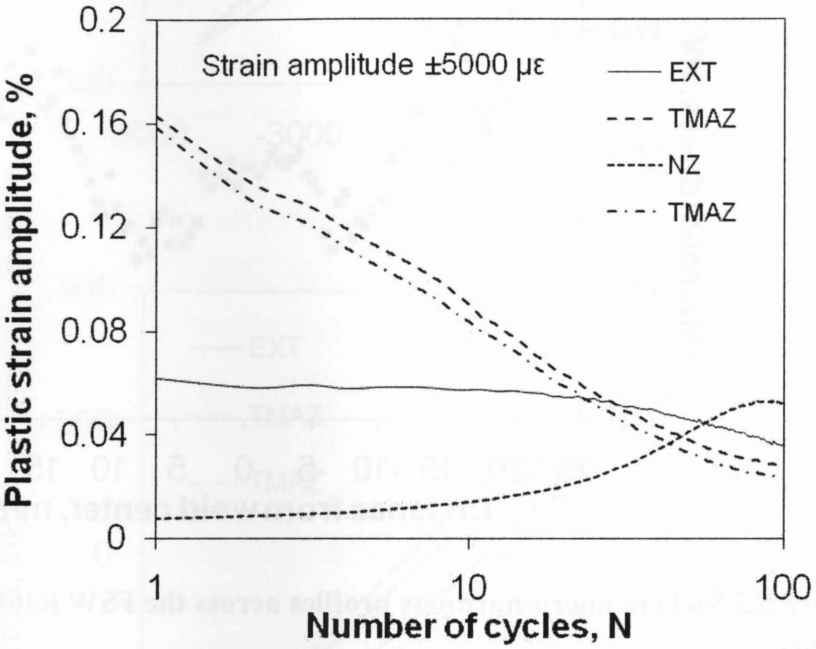

Figure 5.6 Variation of plastic strain amplitudes of the FSWed joint fatigued at a strain amplitude of ±5000 με measured via three FBG sensors and extensometer from the 1st cycle to the 100th cycle.

It is seen from Fig. 5.6 that the plastic strain amplitude measured by the extensometer basically lay in-between those in the NZ and TMAZ, representing an average effect over its gauge length and showing a decreasing trend (cyclic hardening). The overall cyclic hardening, after the initial ~3 cycles, was confirmed by the plot of stress response as a function of cyclic numbers (Fig. 5.7). As cyclic hardening occurred, the stress amplitude had to increase to keep the strain amplitude constant.

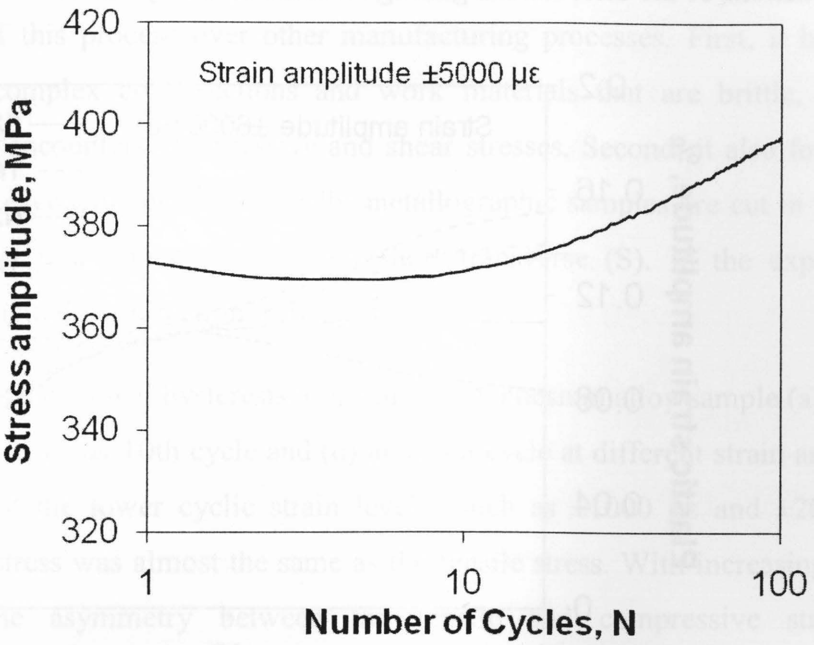

Figure 5.7 Variation of stress amplitudes of the FSWed joint fatigued at a strain amplitude of ±5000 με with the number of cycles.

Since plastic deformation at large strain amplitude is not a completely reversible process, modifications to the structure of the weld joint could occur during cyclic strain. Different fatigue behaviors in NZ and in TMAZ may be explained by their different crystallization structures. As the phenomenon of strain softening following by the strain hardening in NZ has never been reported before, we propose the following explanation. Since NZ experienced a higher temperature in the FSW process, there could be an accumulation of residual stress in NZ. The fatigue cycling released the residual lattice strain that led the strain softening observed. Once the strain-free condition in NZ was reached, the strain hardening process would start like the rest part of the FSW joint. This explanation is corroborated by the cycling test at the strain amplitude of ±6000 με (Fig. 5.8); in which the strain softening reached maximum at ~20th cycle, earlier due to the large strain amplitudes. The difference in plastic strain amplitudes between two zones was also reduce to 0.07 % since the sample had been cycled at lower strain amplitude from ±2000 με to ±5000 με. It is interesting to notice that the two zones reached the same hardness at

~20th cycle. The strain-hardening in fatigue cycling is generally caused by the mutual obstructions of the dislocations gliding on intersection systems.

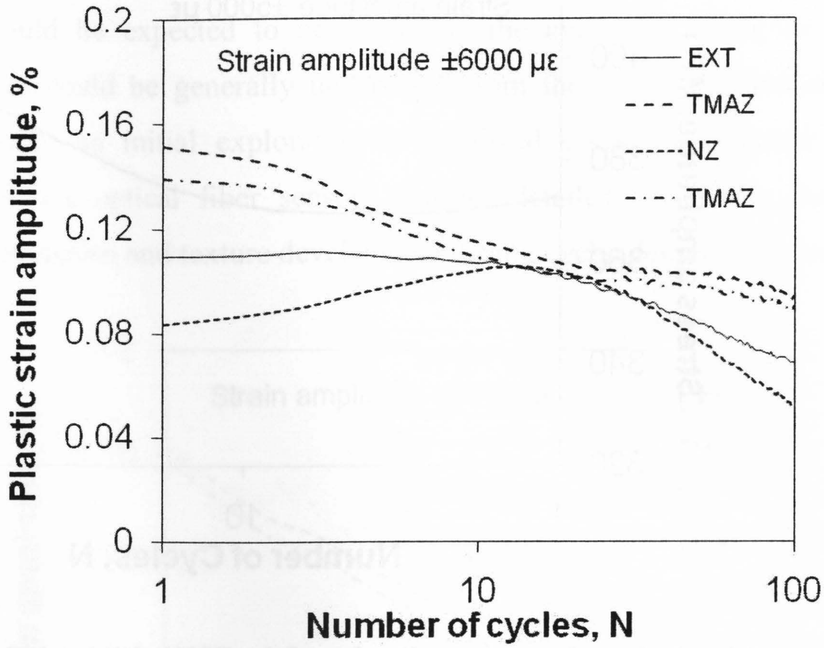

Figure 5.8 Plastic strain amplitudes of three sensors at ±6000 με strain amplitude from the 1st cycle to the 100th cycle.

5.3 Fatigue test of Magnesium extruded alloy AZ31

Due to its lowest density, high specific strength, good castability and weldability, magnesium has been used extensively not only in the nuclear industry, metal and military aircraft, but also in the automotive industry since its significant application in the VW beetle [7]. A report published by the United States Automotive Materials Partnership (USAMP) expressed the vision of increasing the use of magnesium alloys by 340lbs per car by the year 2020, compared to ~10 to 12 lbs of magnesium alloys used in a typical car in 2006 [8]. Currently, the majority of the magnesium alloys used in automotive application is cast alloys because of their high productivity, although wrought magnesium alloys normally provide better properties in terms of strength than the cast magnesium alloys.

Extrusion is a process used to create objects of a fixed cross-sectional profile. A material is pushed or drawn through a die of the desired cross-section. There are two main advantages of this process over other manufacturing processes. First, it has ability to create very complex cross-sections and work materials that are brittle, because the material only encounters compressive and shear stresses. Second, it also forms finished parts with an excellent surface. Normally, metallographic samples are cut in the direction of longitudinal (L), transverse (T), and short transverse (S). In the experiment, the samples in longitudinal direction were used.

Fig. 5.9 shows the typical hysteresis loops of the Magnesium alloy sample (a) at 1st cycle, (b) at 2nd cycle, (c) at 10th cycle and (d) at 100th cycle at different strain amplitude. As we can see, at the lower cyclic strain levels (such as ±1000 με and ±2000 με), the compressive stress was almost the same as the tensile stress. With increasing total strain amplitude, the asymmetry between the tensile and compressive stresses grew substantially. At the higher strain amplitude (such as ±5000 με and ±6000 με) a significant difference between the tensile and compressive stresses appeared. This is basically due to the activity of twinning in compression during the unloading and subsequent detwinning in tension during loading. It was also clearly seen that the 1st cycle hysteresis loops at higher strain amplitudes in Fig. 5.9(a) were more skewed than the 2nd, 10th and 100th cycle hysteresis loops in Fig. 5.9(b-d). This unsymmetrical tensile and compressive yielding phenomenon was Bauschinger-like effect and was associated with the hexagonal crystal structure. Although there are two characteristic deformation mechanisms – sliding and twinning, occurred during plastic deformation of magnesium at room temperature, twinning played an dominant role in the plastic deformation of wrought magnesium alloys.

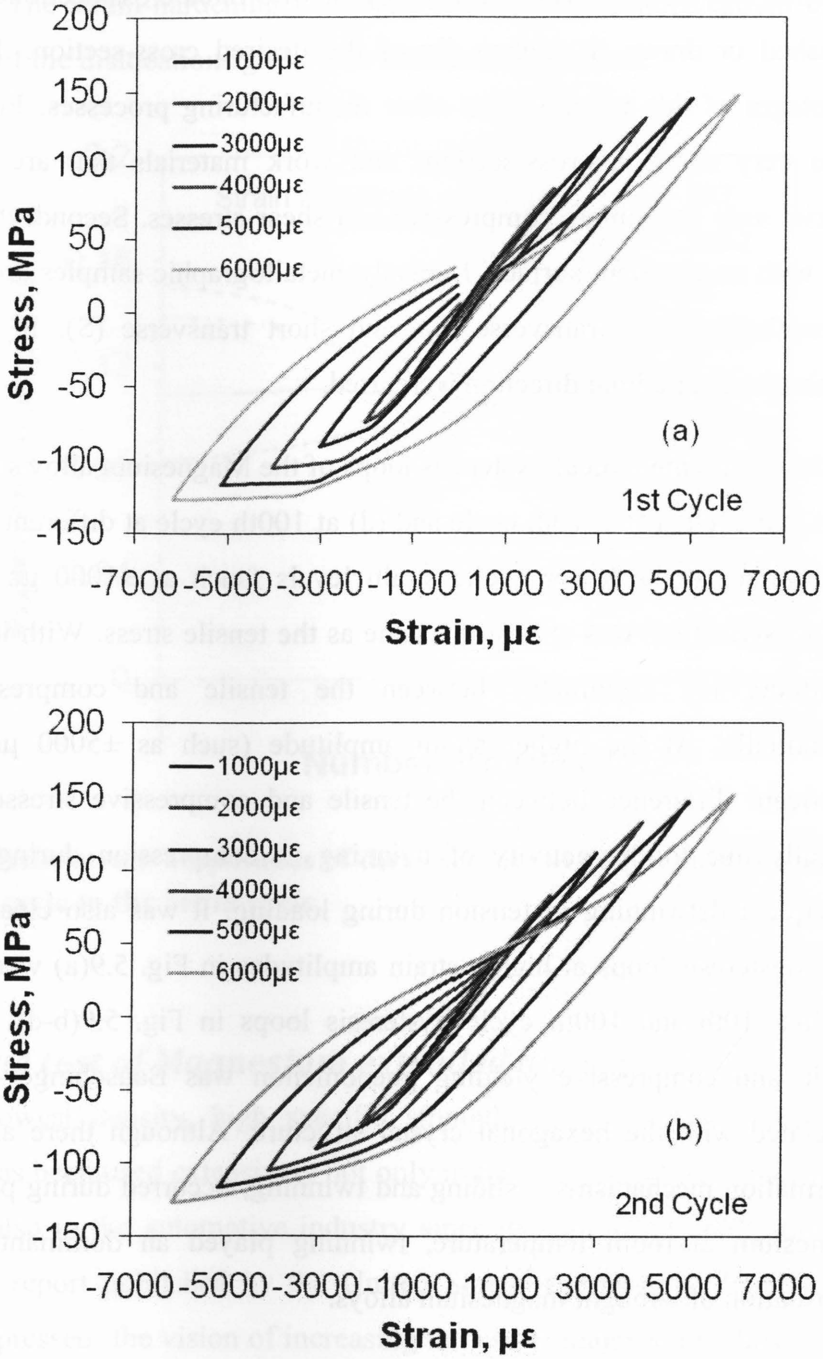
1000με
2000με
3000με
4000με
5000με
6000με
Stress, MPa
Strain, με
(a)
1st Cycle
(b)
2nd Cycle
200
150
100
50
0
-50
-100
-150
-7000 -5000 -3000 -1000 1000 3000 5000 7000

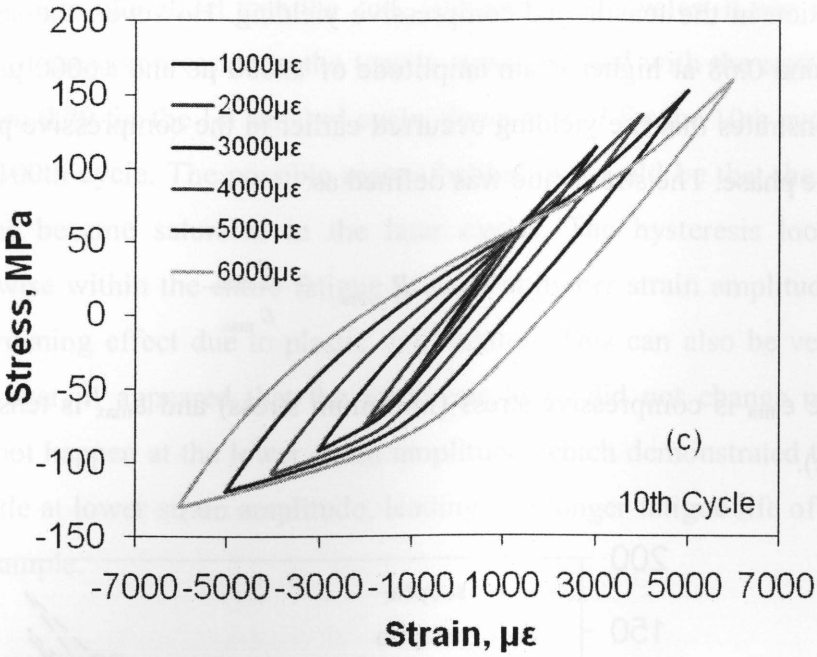

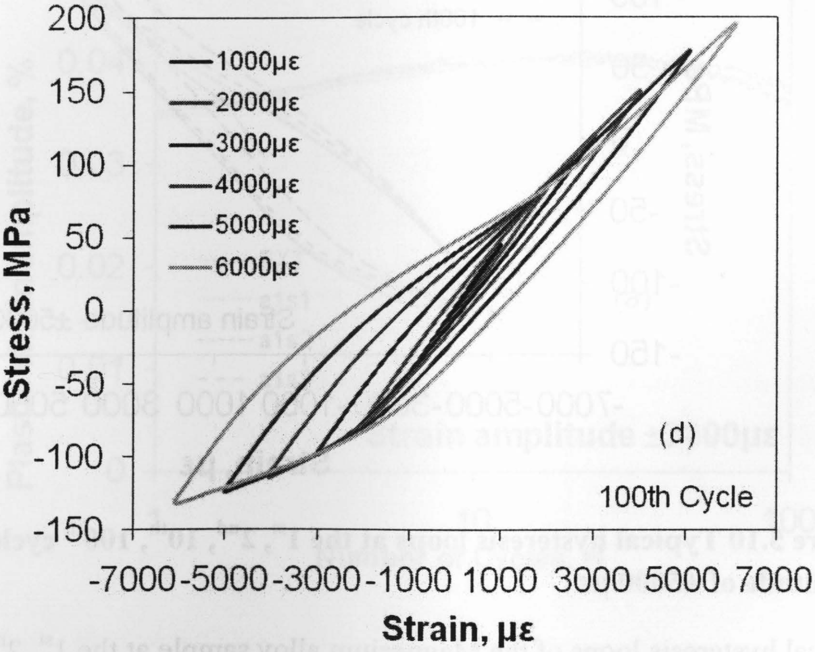

Figure 5.9 Hystesis loops (a) at 1st cycle, (b) at 2nd cycle, (c) at 10th cycle and (d) at 100th cycle for different total strain amplitude from ±1000 με to ±6000 με.

We observed that at lower strain amplitude the Bauschinger effect is not as strong as at higher strain amplitude. At the total strain amplitude of ±1000 με and ±2000 με, the ratio of the compressive to the tensile stress was almost 1, indicating that there was no deviation in the tensile and compressive yielding. However, the stress ratio reduced to 0.70 and 0.68 at higher strain amplitude of ±5000 με and ±6000 με respectively, which demonstrates that the yielding occurred earlier in the compressive phase than that in the tensile phase. The stress ratio was defined as:

$$R_{stress} = \frac{\varepsilon_{\min}}{\varepsilon_{\max}} \tag{5.1}$$

where ε_{min} is compressive stress (minimum stress) and ε_{max} is tensile stress (maximum stress).

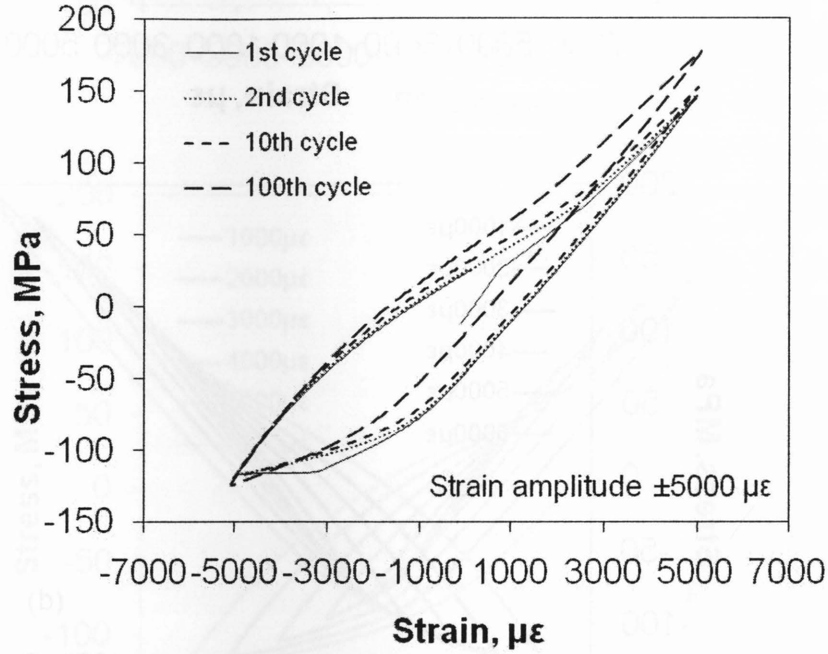

Figure 5.10 Typical hysteresis loops at the 1st, 2nd, 10th, 100th cycle at total strain amplitude of ±5000 με

Typical hysteresis loops of the Magnesium alloy sample at the 1st, 2nd, 10th, 100th cycle of total strain amplitude ±5000 με was shown in Fig. 5.10. It was seen that the tensile stress (maximum stress) increased from 147 MPa at 1st cycle monotonically to 178 MPa at 100th cycle, while the compressive stress (minimum stress) increased from -117 MPa at 1st cycle to -125 MPa concurrently. The change of the tensile stress (31 MPa) is much higher than that of the compressive stress (8 MPa), leading to the very first cycle showed higher Bauschinger-like effect than the 2nd, 10th and 100th cycles. It was also observed that the ratio of the compressive to the tensile stress reduced with the number of cycles increased, from 0.79 for the 1st and 2nd cycle, down to 0.77 for the 10th cycle and end to 0.69 for the 100th cycle. The possible reason behind this could be that the formation of residual twins became saturated in the later cycles. The hysteresis loop twisted in counterclockwise within the entire fatigue process at higher strain amplitude, exhibiting the strain hardening effect due to plastic deformation. This can also be verified in Fig. 5.11(c). However, it appeared that the hysteresis loops did not change much and the twisting did not happen at the lower strain amplitude, which demonstrated the hardening effect was little at lower strain amplitude, leading to a longer fatigue life of the extruded magnesium sample.

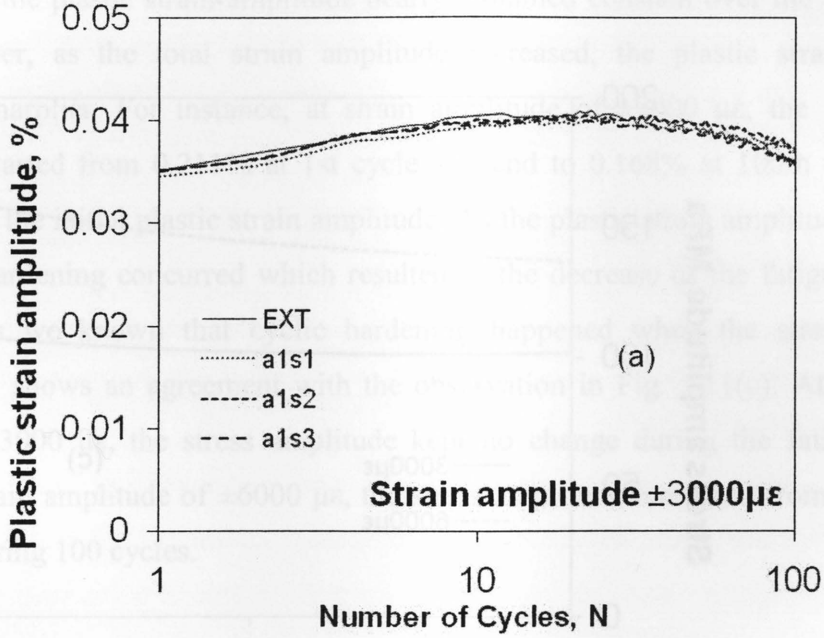

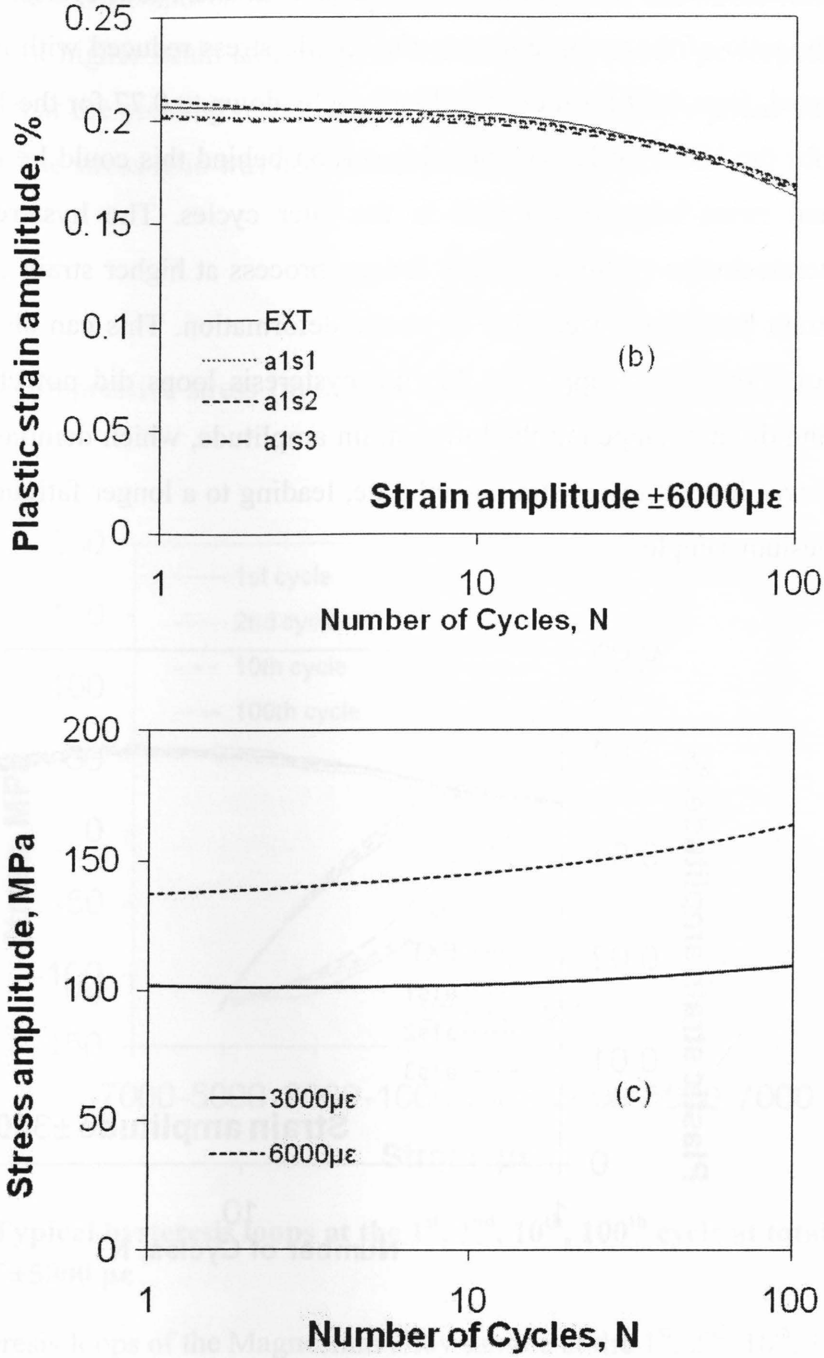

Figure 5.11 Plastic strain amplitudes of three sensors at (a) ±3000 με and (b) ±6000 με strain amplitude from the 1st cycle to the 100th cycle; and (c) Stress amplitude of ±6000 με and ±3000 με strain amplitude from the 1st cycle to the 100th cycle.

It was demonstrated again that a good agreement was observed between the measured plastic strain amplitude from three FBG sensors and that from the extensometer, for all

100 cycles at a cyclic strain amplitude of ±6000 με in Fig. 5.11(b). The largest difference in the plastic strain amplitudes measured by three FBG sensors was about 0.005%, which was only 0.83% of the cyclic strain amplitude of ±6000 με applied. This also clearly validated of the FBG sensors for fatigue testing. The plastic strain amplitude reduced from ~0.20 % at the 1st cycle monotonically to 0.16 % at 100th cycle, indicating cyclic hardening occurred during the fatigue test. Moreover, the plastic strain amplitude ~0.20 % of the magnesium alloys at cyclic strain amplitude of ±6000 με is much higher than that ~0.055 % of the aluminum alloy at cyclic strain amplitude of ±7000 με (Fig. 5.2), which illustrated that the magnesium alloy is much easier to deform than the aluminum alloy under the same fatigue condition.

As shown in Fig. 5.11(a) and (b), at lower strain amplitude (such as ±3000 με), the variation of the plastic strain amplitude nearly remained constant over the entire fatigue life. However, as the total strain amplitude increased, the plastic strain amplitude decreased sharplier. For instance, at strain amplitude of ±6000 με, the plastic strain amplitude started from 0.211% at 1st cycle and end to 0.168% at 100th cycle, 20.4% reduction of the initial plastic strain amplitude. As the plastic strain amplitude decreased, the cyclic hardening concurred which resulted in the decrease of the fatigue life of the material. As we known that cyclic hardening happened when the stress amplitude increased. It shows an agreement with the observation in Fig. 5.11(c). At lower strain amplitude ±3000 με, the stress amplitude kept no change during the fatigue process. While at strain amplitude of ±6000 με, the stress amplitude increased from 137 MPa to 164 MPa during 100 cycles.

Reference

1. W.M. Thomas, E.D. Nicholas, J.C. Needham, M.G. Murch, P. Templesmith, C.J. Dawes, GB Patent Application No. 9125978.8, December 1991.

2. R.S. Mishra, Z.Y. Ma, "Friction stir welding and processing", *Materials Science & Engineering R-Reprots*, vol.50(1-2), pp.1-78, 2005.

3. P.L. Threadgill, A.J. Leonard, H.R. Shercliff, P.J. Withers, "Friction stir welding of aluminium alloys", *International Materials Reviews*, vol.54(2), pp49-93, 2009.

4. R. Nandan, T. DebRoy and H.K.D.H. Bhadeshia, "Recent advances in friction-stir welding - Process, weldment structure and properties", *Progress in Materials Science*, vol.53(6), pp.980-1023, 2008.

5. M. Fairman, N. Afrin, D.L. Chen, X. Cao, M. Jahazi, "Microstructural evaluation of friction stir processed AZ31B-H24 magnesium alloy", *Canadian Metallurgical Quarterly*, vol.46(4), pp.425-432, 2007.

6. N.Afrin, D.L.Chen, X.Cao and M.Jahazi, "Microstructure and tensile properties of friction stir welded AZ31B magnesium alloy", *Materials Science and Engineering A*, vol.472(1-2), pp.179-186, 2008.

7. B.L. Mordike and T. Ebert, "Magnesium - Properties - applications - potential", *Journal of Alloys and Compounds*, vol.336.(1-2), pp.88-113, 2002.

8. S. Begum, D.L. Chen and A.A. Luo, "Strain-Controlled Low-Cycle Fatigue Properties of a Newly Developed Extruded Magnesium Alloy", *Metallurgical and Materials Transactions A*, vol.39(12), pp.3014-3026, 2008.

6 Conclusions and Future Work

6.1 Conclusion

A new FBG-based sensor for the measurements of large cyclic strain variations has been developed. The large contact area between the flat-cladding and substrate, along with the application of a new bonding process, has significantly increased the bonding strength which provided a proper transfer of the strain from substrate to optical fiber. The fatigue tests were carried out on three different types of specimen. Based on the test data, the following conclusion can be drawn.

1. The flat-cladding FBG sensors can be used to measure cyclic strain amplitude as large as ±8000 με in dynamic fatigue tests for aluminum alloys. This represents a remarkable extension of the strain range that could make the FBG sensor a vital tool in the low cyclic fatigue tests at large strain amplitudes.

2. On FSWed specimen, the flat-cladding FBG sensor array detects distinct deformation characteristics occurred in the NZ and across the boundary between TMAZ and HAZ, which illustrated that cyclic hardening in the TMAZ, and softening then hardening in the NZ. The information obtained will help us to better understand the relationship between the fatigue properties and FSW parameters so as to optimize the FSW process.

3. Not limited to FSWed specimen, the flat-cladding FBG sensor also can be used as a vital tool for the in-situ measurements of localized strain which could provide new information unobtainable from the conventional strain gauge or extensometer.

4. On extruded Magnesium specimen, the FBG measurements showed a significant difference between the tensile and compressive yield stresses, leading to asymmetric hysteresis loops at high strain amplitudes due to twinning in compression and subsequent detwinning in tension.

5. Also, on extruded Magnesium specimen, a noticeable counterclock twisting of the stress-to-strain hysteresis loop was observed as number of cycles increase. Higher

Bauschinger-like effect was also detected in the very first cycle because of the saturated formation of residual twins.

6.2 Suggested future work

1. Further improve of the FBG bonding process (epoxy, curing condition etc.) to increase the boding strength between fiber FBG sensors and the sample substrate.
2. Study the last few cycles in fatigue test to find information on crack initiation and propagation.
3. Due to its small size, the FBG sensor could be used to measure the localized strain variations, for example, the welding joints, detect fatigue crack initiation, and determine crack closure effect during fatigue crack propagation.
4. The multiplexed FBG sensor array could also be applied to the measurements of strain distribution in composite materials and mechanical components, as well as for structure health monitoring.

Publications during my MASc studies

1. C. LI, X. Gu, A.H. Feng and D.L. Chen, "Flat-cladding Fiber Bragg Grating Sensors for Large Strain Amplitude Fatigue Tests", to be submitted to *Elsevier, Sensors and Actuators*.

2. C. LI, X. Gu, A.H. Feng and D.L. Chen, "Localized Cyclic Deformation Measurements of Friction Stir Welded Al-Zn-Mg alloy Using a Flat-clad Optical Fiber Sensor Array", submitted to *IEEE Sensors Journal*, August 2009.

3. "Asymmetric Fatigue Tests of Extruded Magnesium Alloy Using Flat-clad Fiber Bragg Grating Sensor Array", in preparation.

2

BL-60-50